Title: MCNP6 Moving Objects. Part II: Simulations

Author(s):   Durkee, Joe W. Jr.
                Johns, Russell C.
                Waters, Laurie S.

Intended for: Progress in Nuclear Energy

MCNP6 MOVING OBJECTS
PART II: SIMULATIONS

by

Joe W. Durkee, Jr., Russell C. Johns, and Laurie S. Waters
Los Alamos National Laboratory
jdurkee@lanl.gov
505-665-0530
Fax: 505-665-2897
PO Box 1663, MS K575
Los Alamos, NM 87545

ABSTRACT

In Part I we presented the theory and code-development upgrades for the new MCNP6

moving-objects feature. This feature facilitates automated execution of radiation transport

simulations in which motion is characterized by rigid-body kinematics for three types of

continuous motion: rectilinear translation, curvilinear translation, and curvilinear rotation.

Models that have complicated motion paths can be simulated using motion-segment

linking. Models that contain up to 1000 moving objects can be executed. In addition,

moving sources and delayed-neutron and delayed-gamma emission due to fission and

activation can be modeled. To illustrate this new capability, we present results for two

sets of test models. The objective of the first set is to demonstrate object motion for a

variety of dynamics conditions. These test models are executed without particle emission

or transport. The updated MCNP6 plotg utility is used to provide numerous plots of

model geometries as they evolve with time. The second set is used to demonstrate object

motion with particle emission and transport. These models examine delayed-gamma

emission induced by thermal neutron irradiation of moving versions of the HEU and Pu

targets used by Beddingfield and Cecil (1998) in experimental work. Our calculated

results show good agreement with the measured delayed-gamma spectra. These results

convey the usefulness of the moving-objects innovation. This new MCNP6 feature allows

realistic simulations of object and/or source motion.

_____

KEYWORDS: MCNP6; moving objects; fission; HEU; Pu, Beddingfield.

1. Introduction

   Monte Carlo techniques permit the study of radiation-transport phenomena in

exquisite detail. Indeed, the Monte Carlo paradigm allows the study of individual

particles as they interact with matter. To accomplish this, cumulative distribution

sampling functions are formed using data such as atom densities, cross-sections, and

emission probabilities. These functions are then sampled to provide particle creation and

transport information such as emission energy, reaction type, etc. Information sampling

for many particles can be used to develop statistical quantifications of behavior, including

average values that can be compared with experimental results.

   MCNP6 (Goorley et al., 2011) is a Monte Carlo particle (radiation quanta)

radiation-transport code that is developed, maintained, and enhanced at Los Alamos

National Laboratory (LANL). Until now, MCNP6 could not accommodate simulations

involving motion. In Part I, we presented the theory that has been developed to treat

object motion in MCNP6. That presentation discusses the concepts of and derived

equations for rigid-body kinematics involving rectilinear translation, curvilinear

translation, and curvilinear rotation as well as the implementation of the motion

capability in MCNP6. In addition, upgrades to permit modeling of moving sources and

delayed-particle emission were delineated.

The complicated assortment of object and/or source motion simulation capabilities

that are incorporated in the MCNP6 moving-objects feature renders verification and

validation efforts challenging. We report here initial progress regarding these efforts.

Two sets of models are used. The first set involves only object motion. These models

exclude radiation transport. The second set involves object motion and delayed-gamma

production related to measurements reported by Beddingfield and Cecil (1998) involving

stationary HEU and Pu targets.

2.   Results

Our first set of models is designed to demonstrate object-motion functionality. The

four models we present include (1) rectilinear translation, (2) curvilinear rotation in the

x^G-y^G plane, (3) curvilinear rotation for a tilted plane, and (4) "horseshoe" motion. In

each model, the objects are aluminum boxes that are moved in vacuum. This set of

models addresses code verification regarding object motion.

The second set of models contains two pseudo-validation calculations related to

experimental measurements of delayed-gamma emission (Beddingfield and Cecil, 1998).

The first model has an HEU target, and the second a Pu target. Each target moves in a

vacuum and is irradiated by a beam of thermal neutrons. We compare the measured and calculated delayed-gamma emission data.

Generally speaking, visualization of the object motion is best appreciated when the geometry plots are displayed to the computer screen using the new plotg "time" command to plot a sequence of images. Our results include images of object motion at a sequence of times created using the plotg utility.

2.1. Test Model 1. Rectilinear translation

Test Model 1 consists of two moving square boxes, each of which extends 300 cm on each side and has 1-cm-thick aluminum walls. The boxes are inside of a third stationary rectangular box that extends 700 cm in the x^G and y^G directions and from –5100 to 5100 cm in the z^G direction. Box 3 is inside of a stationary 6000-cm-radius sphere. The boxes and the sphere are voided. At time zero the square boxes are centered at $x^G = y^G =0$, with box 1 at $z^G =$–4400 cm and box 2 at $z^G =$–4900 cm. Boxes 1 and 2 move along a single motion segment via rectilinear translation in the $+z^G$ direction with initial velocities of 880 and 440 cm/s, respectively. Box 1 moves at constant velocity, while box 2 experiences a constant acceleration of 80 cm/s^2. Table 1 lists the model data.

Table 1. Test Model 1 data.

Quantity	Variable	Box 1 Data	Box 2 Data
Global x location at $t=0$	O_x^G (cm)	0	0
Global y location at $t=0$	O_y^G (cm)	0	0
Global z location at $t=0$	O_z^G (cm)	–4.4d3	–4.9d3
Linear velocity in x^P direction	v_x (cm/s)	0	0
Linear velocity in y^P direction	v_y (cm/s)	0	0
Linear velocity in z^P direction	v_z (cm/s)	8.8d2	4.4d2
Linear acceleration in x^P direction	a_x (cm/s^2)	0	0
Linear acceleration in y^P direction	a_y (cm/s^2)	0	0
Linear acceleration in z^P direction	a_z (cm/s^2)	0	8.0d1
Start time	t_0 (s)	0	0
End time	t_e (s)	1.0d1	1.0d1

Table 2 lists the object orientation coefficients $B_1^{GL} - B_9^{GL}$ for the two moving boxes.

The orientation coefficients are the same for Box 1 and 2, and they align the box axes x^L,

y^L, and z^L with the global-coordinate axes x^G, y^G, and z^G. The path orientation

coefficients for each object, $B_1^{GP} - B_9^{GP}$, are identical to the object-orientation

coefficients.

Table 2. Test Model 1 object orientation coefficients for Box 1 and Box 2.

B_1^{GL}	1
B_2^{GL}	0
B_3^{GL}	0
B_4^{GL}	0
B_5^{GL}	1
B_6^{GL}	0
B_7^{GL}	0
B_8^{GL}	0
B_9^{GL}	1

Figure 1 shows the geometry at 0, 5, and 10 s. Box 1 (red) initially moves away from Box 2 (dark blue). Box 2 accelerates to approach Box 1 as the simulation proceeds. Table 3 lists calculated locations at 5 and 10 s.

Table 3. Test Model 1 calculated location data at 5 and 10 s.

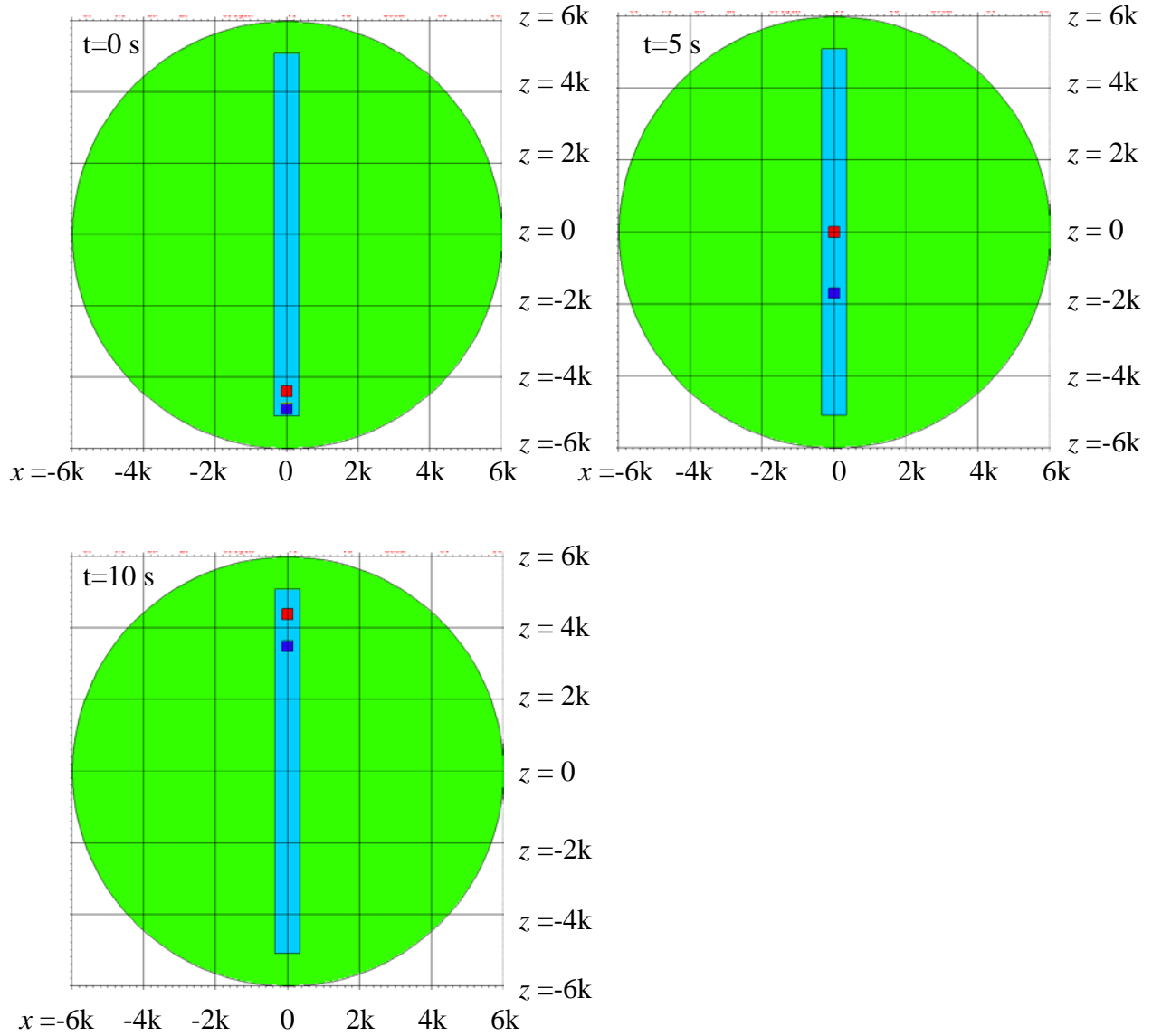| Quantity	Variable	Box 1 Data	Box 2 Data
Global x location at t=5 s	R_x^G (cm)	0	0
Global y location at t=5 s	R_y^G (cm)	0	0
Global z location at t=5 s	R_z^G (cm)	0	−1.7d3
Global x location at t=10 s	R_x^G (cm)	0	0
Global y location at t=10 s	R_y^G (cm)	0	0
Global z location at t=10 s	R_z^G (cm)	4.4d3	3.5d3

Figure 1. Test Model 1. Box 1 (red) and Box 2 (dark blue) undergoing rectilinear translation at t=0, 5, and 10 s. Locations in "k" thousands of cm.

2.2. Test Model 2. Curvilinear rotation in the x^G-y^G plane.

Test Model 2 is identical to Test Model 1 except for the parameters that describe the

motion of Box 1. Box 1 experiences curvilinear rotation in the plane $z^G =12$ cm parallel

to the $x^G - y^G$ plane. The axis-of-rotation for Box 1 is located at $O_{Ax}^G = 400$ cm,

$O_{Ay}^G = 500$ cm, $O_{Az}^G = 12$ cm, and the radius-of-curvature is $\rho = \left| \vec{r}^P(t) \right| = 4400$ cm. Box 1 is

initially located at $O_x^G = 4800$ cm, $O_y^G = 500$ cm, $O_z^G = 12$ cm. Box 1 moves with a

constant angular velocity of 0.2π rad/s, rotating once around its circular path in 10 s.

Table 4 lists the model parameters for Box 1. Table 5 lists the path orientation data for

each box. Table 6 lists the calculated locations at 5 and 10 s.

Table 4. Test Model 2 data for Box 1.

Quantity	Variable	Box 1 Data
Global x location at t=0	O_x^G (cm)	4.8d3
Global y location at t=0	O_y^G (cm)	5.0d2
Global z location at t=0	O_z^G (cm)	1.2d1
Axis of rotation global x location	O_{Ax}^G (cm)	4.0d2
Axis of rotation global y location	O_{Ay}^G (cm)	5.0d2
Axis of rotation global z location	O_{Az}^G (cm)	1.2d1
Angular velocity	ω (rad/s)	6.283185307d-1
Angular acceleration	α (rad/s^2)	0.0
Start time	t_0 (s)	0.0
End time	t_e (s)	1.0d1

Table 5. Test Model 2 path orientation data for Box 1 and Box 2.

B_1^{GP}	1
B_2^{GP}	0
B_3^{GP}	0
B_4^{GP}	0
B_5^{GP}	1
B_6^{GP}	0
B_7^{GP}	0
B_8^{GP}	0
B_9^{GP}	1

Table 6. Test Model 2 calculated location data at 5 and 10 s.

Quantity	Variable	Box 1 Data	Box 2 Data
Global x location at t=5 s	R_x^G (cm)	–4.0d3	0
Global y location at t=5 s	R_y^G (cm)	5.0d2	0
Global z location at t=5 s	R_z^G (cm)	1.2d1	1.7d3
Global x location at t=10 s	R_x^G (cm)	4.8d3	0
Global y location at t=10 s	R_y^G (cm)	5.0d2	0
Global z location at t=10 s	R_z^G (cm)	1.2d1	3.5d3

The curvilinear motion experienced by Box 1 is calculated using Eqs.(46) and (62) of
Part I; these equations are used to determine the box's location and orientation,
respectively. Figure 2 shows Box 1 at 60-degree intervals (~1.66-s intervals) as it moves
from time 0 to 10 s. Box 1 (red) is located in the $x^G - y^G$ plane at z^G = 12 cm. Box 1
rotates around Box 3 (light blue) with the axis-of-rotation (at O_{Ax}^G=400, O_{Ay}^G=500) offset
from the axis of Box 3 (centered at at $O_x^G = 0$, $O_y^G = 0$). The side of Box 1 that initially
faces its axis-of-rotation continues to face its axis-of-rotation throughout the simulation.
This motion occurs simultaneously with that of Box 2, which moves in the $+z^G$ direction

inside of Box 3. We mention that the user must create the geometry so that a moving

object does not collide with a static object or another moving object.[†]

[†] Collisions will cause geometry errors the produce lost particles and/or code crashes during execution.
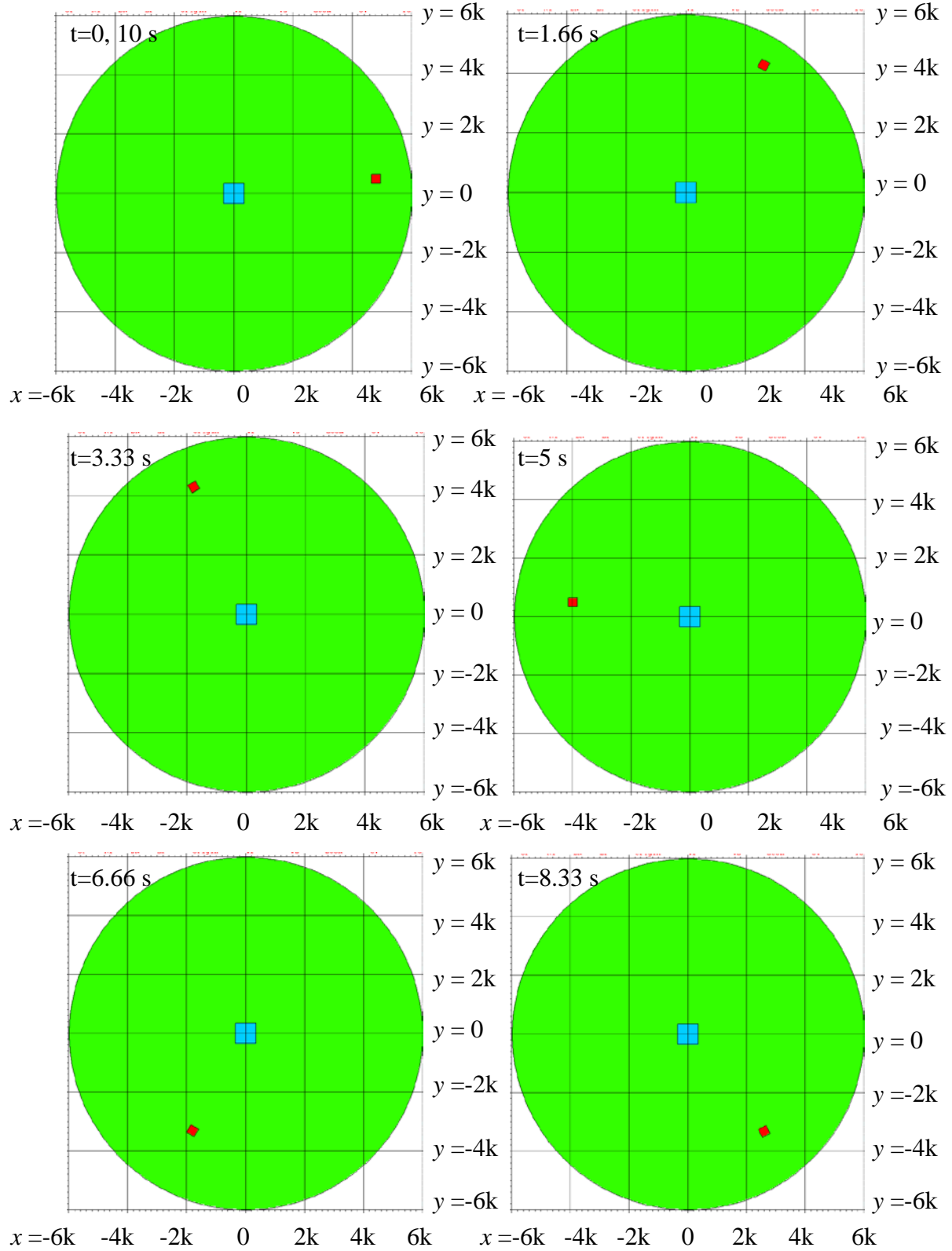
Figure 2. Test Model 2. Box 1 undergoing curvilinear rotation at t=0, 1.66s, 3.33, 5, 6.66, 8.33, and 10 s. Locations in "k" thousands of cm. The plot view is the $x^G - y^G$ plane at $z^G = 12$ cm.

Figure 3 shows the geometry in the $x^G - y^G$ plane at $z^G = 12$ cm at time 6.9 s. This

image includes Box 2 (dark blue) as it passes through at $z^G = 12$ cm inside of Box 3 (light
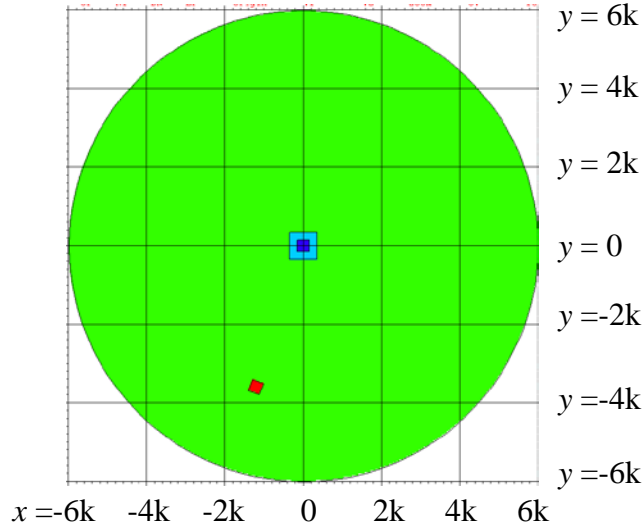
blue).

Figure 3. Test Model 2. Model geometry at t = 6.9 s. Box 1 (red) is undergoing
curvilinear rotation, while Box 2 (dark blue) experiences rectilinear translation as moves
through the plot plane. Locations in "k" thousands of cm. The plot view is the
$x^G - y^G$ plane at $z^G = 12$ cm.

Figure 4 shows the geometry at 0, 5.15, 5, 9.85, and 10 s in the $x^G - z^G$ plane at $y^G = 0$

cm. Because Box 1 is outside of Box 3, only Box 2 moves through Box 3. Box 1 appears

in the images circa 5.15 and 9.85 s as it passes below (into page) and above (out of page)
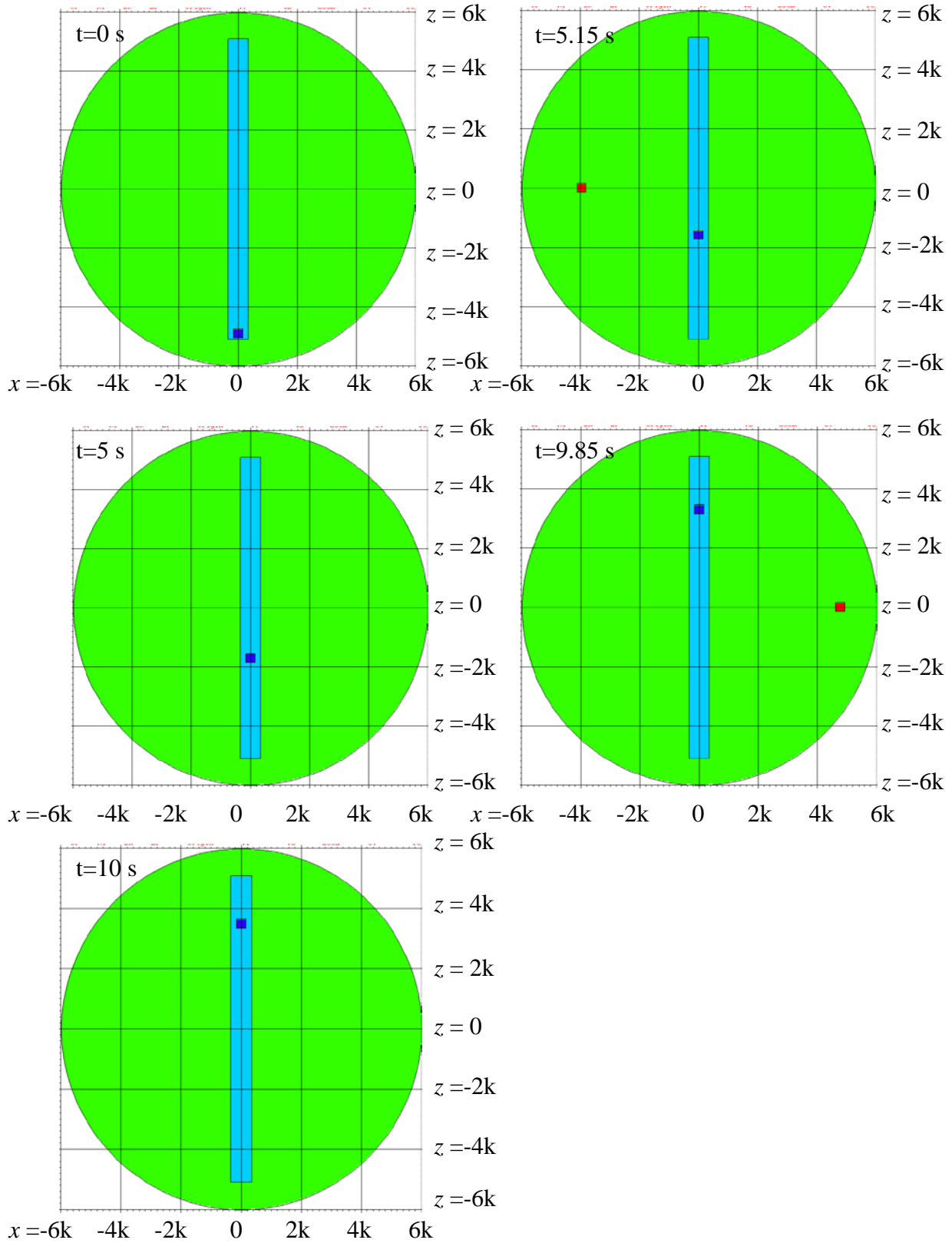
the $x^G - z^G$ plane.

Figure 4. Test Model 2. Geometry at t = 0, 5.15, 5, 9.85, and 10 s. Box 1 (red)
experiencing curvilinear rotation, Box 2 (dark blue) undergoing rectilinear translation.
Locations in "k" thousands of cm. The plot view is the $x^G - z^G$ plane at $y^G = 0$ cm.

2.3. Test Model 3: Curvilinear rotation in slanted plane.

Test Model 3 is like Test Model 1 exclusive of the motion assigned to Box 1. Box 1

experiences curvilinear rotation on a circular path in a tilted plane as shown in Fig. 5. The

plane's orientation is prescribed in terms of intersections with the x^G, y^G, z^G axes at a^G,
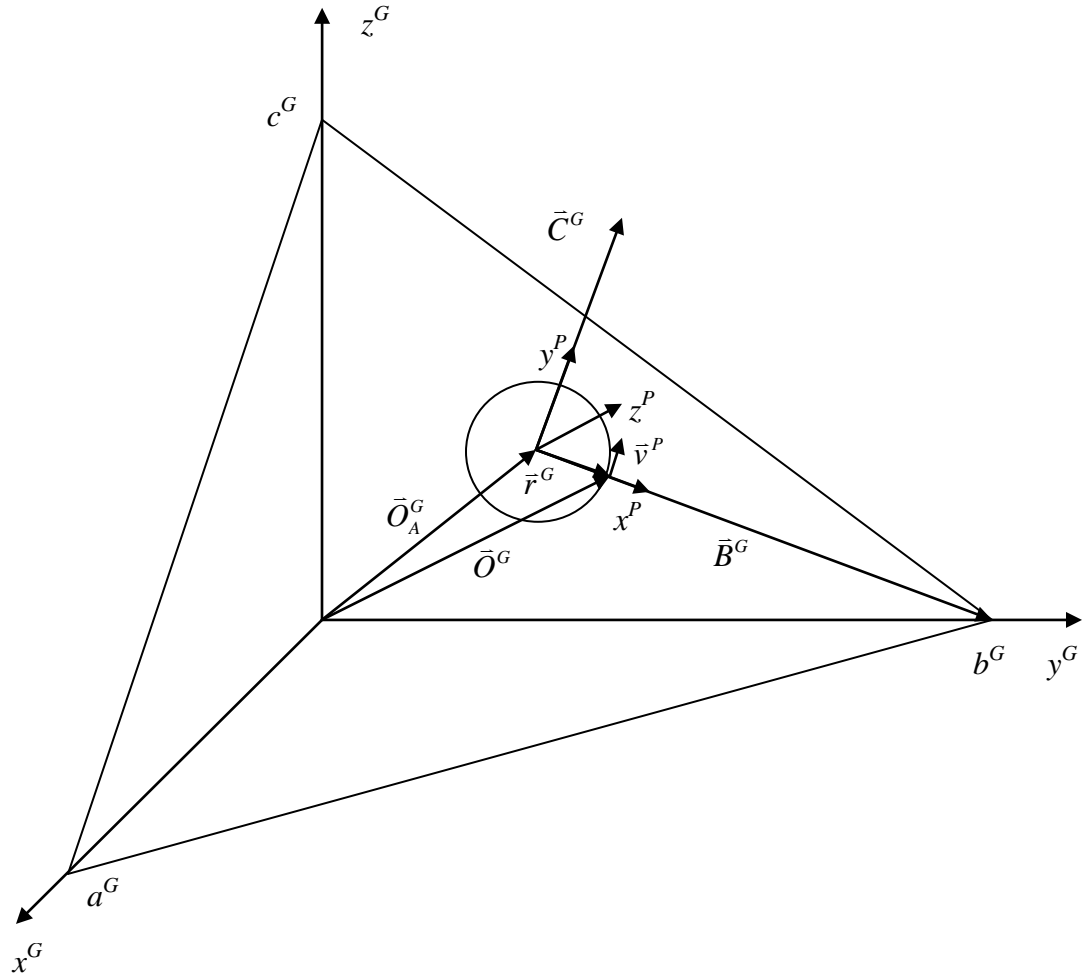
b^G and c^G.

Figure 5. Test Model 3 path for Box 1. Object curvilinear rotation about a fixed axis in

the plane intersecting the points $x^G = a^G$, $y^G = b^G$, $z^G = c^G$. $\vec{O}^G$ and $\vec{O}_A^G$ are the object's

location at time $t = 0$ and axis of rotation, respectively. The radius-of-curvature is

$\rho = \left| \vec{r}^G(t) \right|$, which is constant. The object starts at $\vec{O}^G$ with velocity $\vec{v}^P$. The path is

oriented in terms of the cosines of the angles $B_1^{GP} - B_9^{GP}$ between the global-coordinate

axes x^G, y^G, and z^G and the path's axes x^P, y^P, and z^P.

Stipulated input data for Box 1 are listed in Table 7. The angular velocity is selected

so that Box 1 makes one revolution along its path in 10 s. Calculated (see Appendix)

location data for Box 1 are given in Table 8. Table 9 contains the calculated (see

Appendix) path orientation data $B_1^{GP} - B_9^{GP}$.

Table 7. Test Model 3 stipulated input data for Box 1.

Quantity	Variable	Box 1 Data
Path intersection with x^G axis	a^G (cm)[†]	2.0d4
Path intersection with y^G axis	b^G (cm)	2.5d4
Path intersection with z^G axis	c^G (cm)	3.0d4
Radius-of-curvature ρ (cm)	ρ (cm)	4.4d3
Axis-of-rotation global x location	O_{Ax}^G (cm)	1.0d4
Axis-of-rotation global y location	O_{Ay}^G (cm)	1.2d4
Angular velocity	ω (rad/s)	6.283185307d-1
Angular acceleration	α (rad/s^2)	0.0
Start time	t_0 (s)	0.0
End time	t_e (s)	10.0

Table 8. Test Model 3 calculated input values for Box 1.

Quantity	Variable	Equation	Box 1 Data
Axis of rotation global z location	O_{Az}^G (cm)	Eq.(10)	6.0d2
Global x location at t=0	O_x^G (cm)	Eq.(15)	7.31906599d3
Global y location at t=0	O_y^G (cm)	Eq.(15)	1.54852142d4
Global z location at t=0	O_z^G (cm)	Eq.(15)	4.39143959d2

[†] See Fig.4 for meaning of a^G, b^G, and c^G.

Table 9. Test Model 3 calculated path orientation data for Box 1.

Cosine of angle	Value
B_1^{GP}	–0.609303185
B_2^{GP}	0.792094140
B_3^{GP}	–0.036558191
B_4^{GP}	–0.386012296
B_5^{GP}	–0.256028563
B_6^{GP}	0.886252719
B_7^{GP}	0.692635645
B_8^{GP}	0.554108516
B_9^{GP}	0.461757097

For Box 1, the object orientation data $B_1^{GL} - B_9^{GL}$ at time zero are selected to be identical to the path orientation data $B_1^{GP} - B_9^{GP}$ listed in Table 9. Selection of these object-orientation data for Box 1 has the effect of allowing Box 1 to appear as a square in the geometry plots as the object rotates around its axis-of-rotation on the slanted path. Equation (58) of Part I is used to calculate the orientation of Box 1 as a function of time, while its location is calculated using Eq.(40) of Part I. The time-invariant $B_1^{GL} - B_9^{GL}$ for Box 2 are listed in Table 3.

Table 10 contains the calculated locations of Box 1 at several times.

Table 10. Test Model 3 calculated Box 1 location data.

Time	$R_x^G(t)$ (cm)	$R_y^G(t)$ (cm)	$R_z^G(t)$ (cm)
0, 10.0	7.31906599d3	1.54852142d4	4.39143959d2
1.666	7.18862859d3	1.27670073d4	3.89664839d3
3.333	9.86956254d3	9.28179309d3	4.05750448d3
5.0	1.26809340d4	8.51478578d3	7.60856041d2
6.666	1.28113715d4	1.12329926d4	-2.69664832d3
8.333	1.01304381d4	1.47182065d4	-2.85750482d3

Figure 6 shows Box 1 at 60-degree intervals (~1.66 s intervals) as it moves in the

tilted plane from time 0 to 10 s.[†] Box 1 (red) rotates around its axis-of-rotation $O_{Ax}^{G} =$

10000 cm, $O_{Ay}^{G} = 12000$ cm, $O_{Az}^{G} = 600$ cm. The side of Box 1 that initially faces its axis-

of-rotation continues to face its axis-of-rotation throughout the simulation. The motion of

Box 2 is as in Fig. 13 for Test Model 2.

[†] The plots are generated by setting the MCNP6 plotg utility origin to O_{Ax}^{G}, O_{Ay}^{G}, O_{Az}^{G} values in Tables 7 and 8 and the basis to $B_{1}^{GP} - B_{9}^{GP}$ values in Table 9. This centers the plotter at the axis-of-rotation in the plane of the motion path.
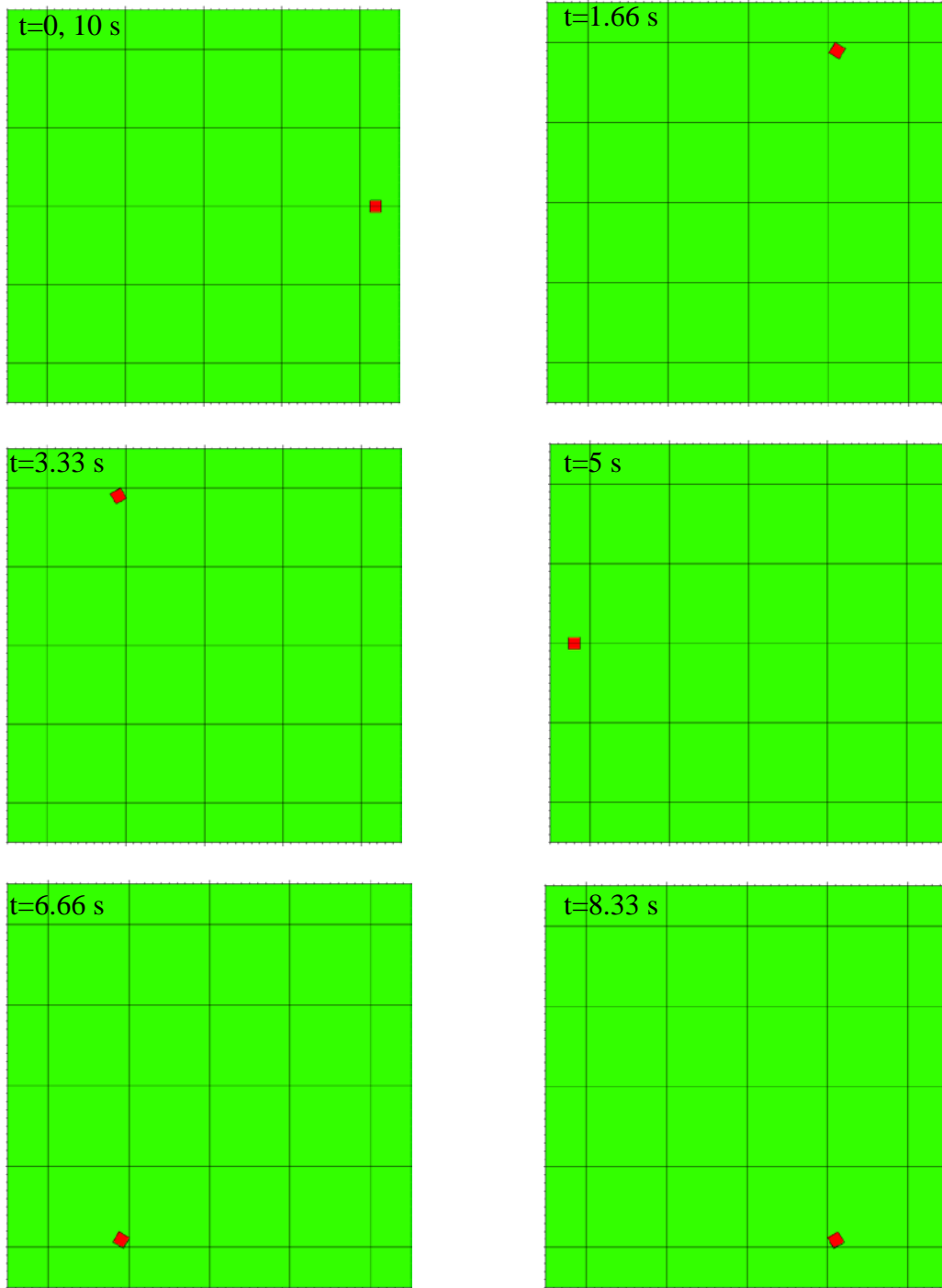
Figure 6. Test Model 3. Box 1 undergoing curvilinear rotation in tilted plane at t=0, 1.66s, 3.33, 5, 6.66, 8.33, and 10 s. Axis-of-rotation $O_{Ax}^{G} = 10000$ cm, $O_{Ay}^{G} = 12000$ cm, $O_{Az}^{G} = 600$ cm is located at the center of each figure. Box 1 locations are given in Table 10.

2.4. Test Model 4. Horseshoe motion and motion-segment linking

This simulation illustrates motion-segment linking and the simultaneous motion of three boxes. The duration of motion is 10 s for each box. Box 1 moves in the $x^G - y^G$ plane at $z^G = 0$ with motion that resembles the shape of a horseshoe. Box 2 motion is the same as for Test Model 1, i.e., constant-velocity motion along the z^G axis in the $+z^G$ direction. Box 3 moves in the $x^G - y^G$ plane experiencing rectilinear translation in the $+x^G$ direction.

The motion of Box 1 is characterized using three linked motion segments: (1) rectilinear translation in the $+y^G$ direction, (2) counterclockwise curvilinear translation, and (3) rectilinear translation in the $-y^G$ direction. Box 1 moves with a constant velocity in motion segments 1 and 2. Box 1 decelerates to a stop between the time it exits motion segment 2 and 10 s.

Table 11 contains the location and dynamics data for Box 1 in motion segments 1 and 3 and the data for Box 3. For this simulation, the time and global-coordinate locations of the objects at the beginning of each motion segment are input. The path axes x^P, y^P, and z^P for each box are aligned with the global-coordinate axes x^G, y^G, and z^G so that the $B_1^{GP} - B_9^{GP}$ are the quantities listed in Table 6. The object orientation data $B_1^{GL} - B_9^{GL}$ for each box are identical to the $B_1^{GP} - B_9^{GP}$ values. The positive sign for the linear acceleration a_y of Box 1 in motion segment 3 causes deceleration because Box 1 is

moving in the $-y^G$ direction. Table 12 lists the Box 1 data for motion segment 2. Box 3

moves with constant velocity in the $+x^G$ direction.

Table 11. Test Model 4 data for Box 1 in motion segments 1 and 3 and Box 3.

Quantity	Variable	Box 1 Mot. Seg. 1	Box 1 Mot. Seg. 3	Box 3 Data
Global x location at t_0	O_{Ax}^G (cm)	3.0980d3	5.0d1	-3.3d3
Global y location at t_0	O_{Ay}^G (cm)	5.0d1	3.7076d3	2.0d3
Global z location at t_0	O_{Az}^G (cm)	0	0	0
Linear velocity in x^P direction	v_x (cm/s)	0	0	0
Linear velocity in y^P direction	v_y (cm/s)	1.78816d3	-1.78816d3	6.6d2
Linear velocity in z^P direction	v_z (cm/s)	0	0	0
Linear acceleration in x^P direction	a_x (cm/s^2)	0	0	0
Linear acceleration in y^P direction	a_y (cm/s^2)	0	3.388558795d2	0
Linear acceleration in z^P direction	a_z (cm/s^2)	0		8.0d1
Start time of segment	t_0 (s)	0	4.72294828d0	0
End time of segment	t_e (s)	2.04545454d0	1.0d1	1.0d1

Table 12. Test Model 4 data for Box 1 in motion segment 2.

Quantity	Variable	Box 1 Data
Global x location at t=2.04545454 s	R_x^G (cm)	3.098d3
Global y location at t=2.04545454 s	R_y^G (cm)	3.7076d3
Global z location at t=2.04545454 s	R_z^G (cm)	0
Axis of rotation global x location	O_{Ax}^G (cm)	1.574d3
Axis of rotation global y location	O_{Ay}^G (cm)	3.7076d3
Axis of rotation global z location	O_{Az}^G (cm)	0
Angular velocity	ω (rad/s)	1.17333333d0
Angular acceleration	α (rad/s^2)	0
Start time of segment	t_0 (s)	2.04545454d0
End time of segment	t_e (s)	4.72294828d0

Figure 7 shows the motion of Box 1 and Box 2 in the $y^G - z^G$ plane at t=0, 6, 7, 8, 9, 10 s. Box 1 becomes visible in the sequence of figures around the time of the end of its second motion segment as it nears the y^G axis and its size causes it to straddle y^G axis. Box 1 then moves in its third motion segment via rectilinear translation as it decelerates to a stop. Box 2 accelerates in rectilinear translation in the $+z^G$ direction. Boxes 1 and 2 avoid collision.
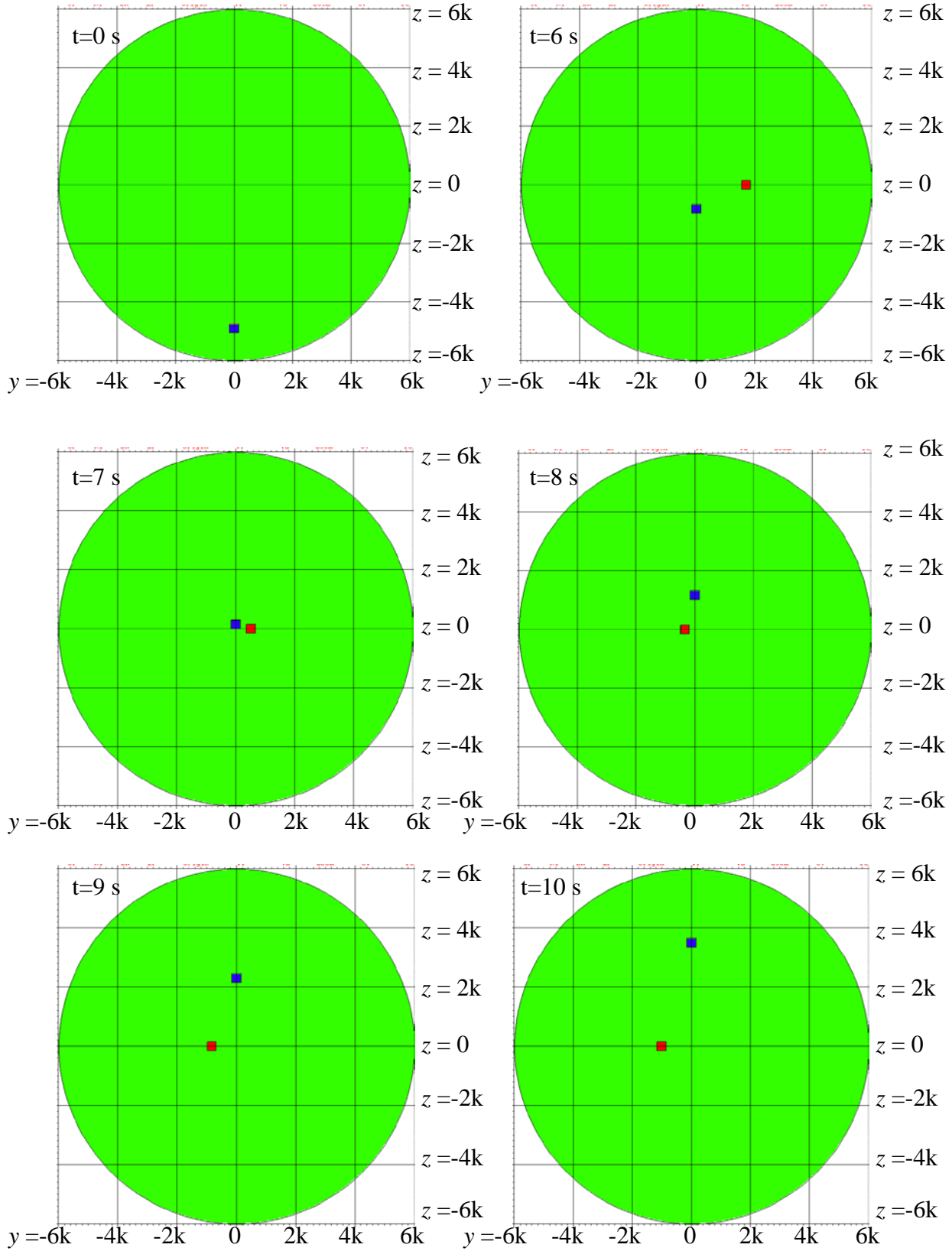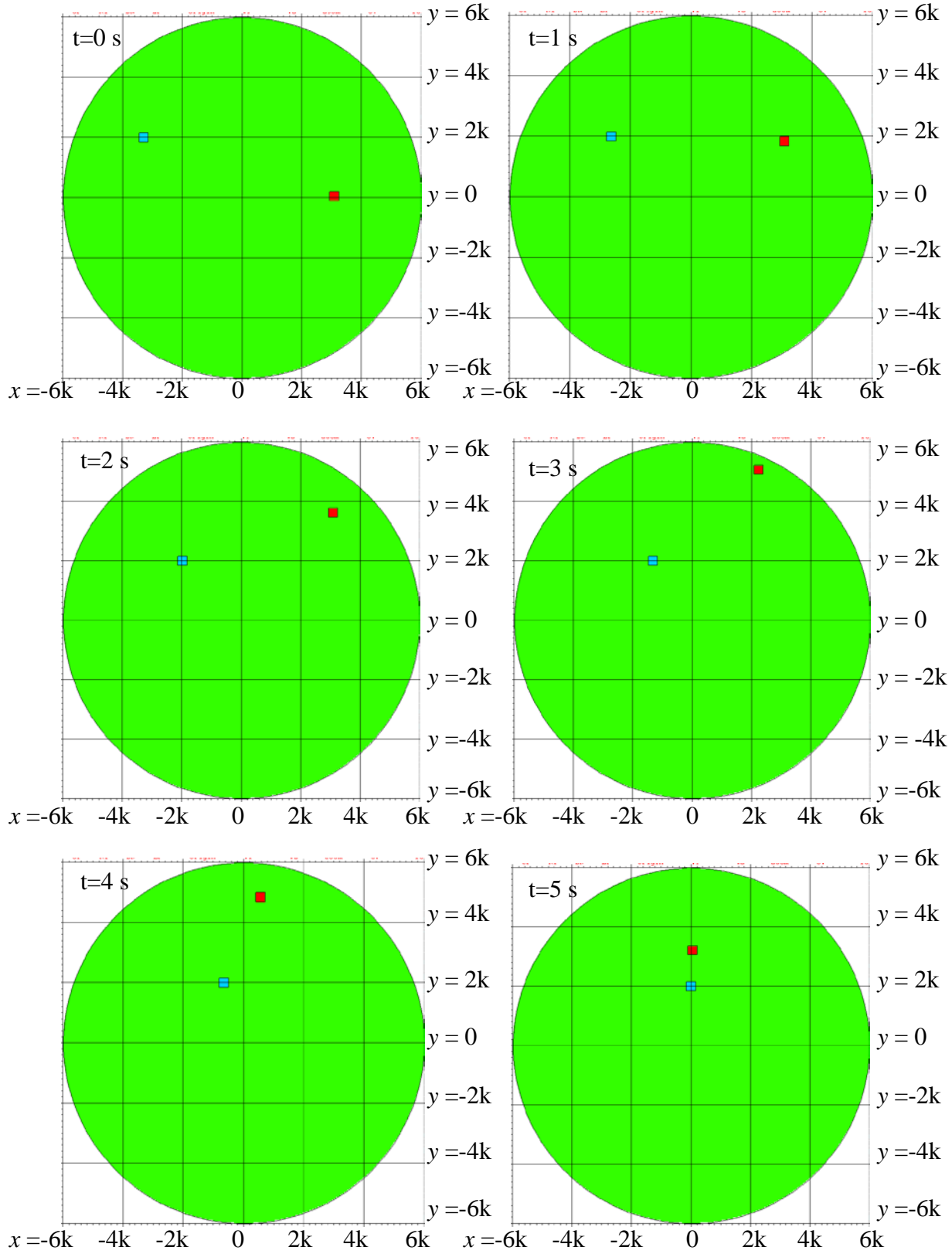
Figure 7. Test Model 4. Box 1 (red) and Box 2 (dark blue) motion in y^G –z^G plane at t=0, 6, 7, 8, 9, 10 s. Locations in "k" thousands of cm.

Figure 8 shows the motion of Box 1 and Box 3 in the $x^G - y^G$ plane at t=0, 6, 7, 8, 9, 10 s. Box 1 experiences horseshoe motion as it initially moves at constant velocity in the $+y^G$ direction, then moves counterclockwise through 180 degrees, and then decelerates in the $-y^G$ direction to come to a stop. Box 3 moves via rectilinear translation in the $+x^G$ direction. Boxes 1 and 3 do not collide.
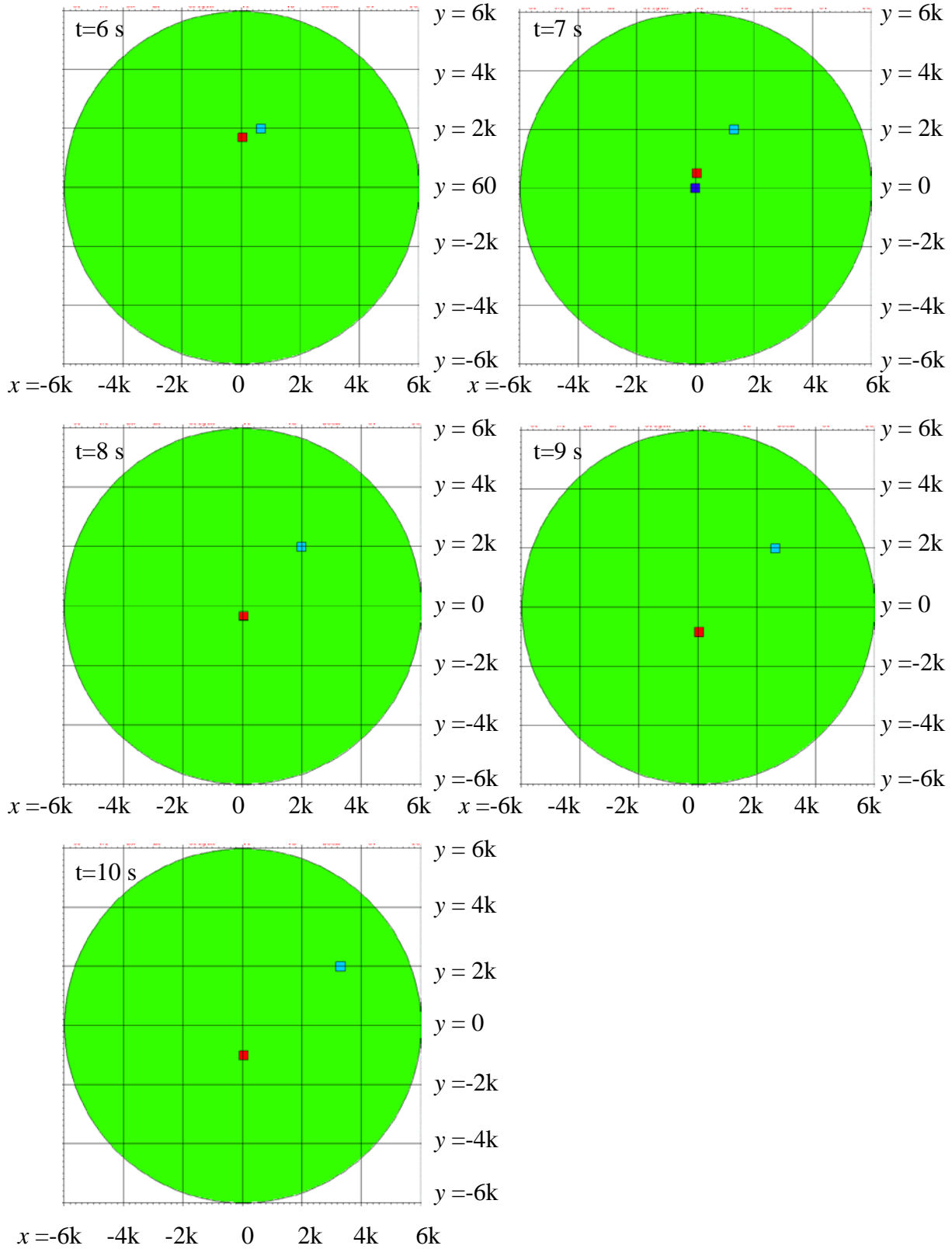
Figure 8. Test Model 4. Box 1 (red) and Box 3 (light blue) motion in $x^G - y^G$ plane at 1-second intervals from t=0 to 10 s. Locations in "k" thousands of cm.

2.5. Pseudo-validation calculations

In previous work (Durkee et al., 2009), we reported simulation results pertaining to

the delayed-gamma experiments reported by Beddingfield and Cecil (1998). The

experiments involved the irradiation of stationary HEU and Pu targets by a moderated

^{252}Cf neutron source. Because many of the details of their experiments were not provided,

in our simulations we approximated the experimental setup by using a 0.025-eV neutron

pulse directed inwardly from a spherical surface source. In addition, because details of

their HPGe detector were unavailable, we developed a simulated detector using

representative parameters. Despite our modeling approximations, our simulation results

agreed well with their measured spectra for HEU and Pu.

Here we modify our earlier (Durkee et al., 2009) HEU and Pu models to incorporate

motion. Our objective is twofold. First, we seek pseudo-validation results. We rely on

adaptations of our static models and the use of the Beddingfield and Cecil (1998) data

based on the premise that, subject to the conditions of the moving-objects feature and our

models, the delayed-gamma emission spectra emitted due to irradiation of static and

moving HEU and Pu targets should be indistinguishable.

Second, the configuration and parameters used in our models are designed to highlight

the capabilities and limitations of the moving-objects feature. The capabilities used here

include object motion and delayed-particle emission. An important underlying

component of this pair of capabilities as well as source and prompt particles is

verification that MCNP6 does not encounter difficulties tracking particles through

geometry. MCNP6 has powerful capabilities to discern problematic issues during

particle transport and issue alerts if particles become "lost." These test problems exercise

these tracking capabilities for source, prompt, and delayed particles in moving

geometries.

   The selected configuration and parameters for the two models serve to highlight the

potential limitation regarding Stipulation 4 of Part I: the geometry is updated to the time

at which a source or delayed particle is emitted and then held fixed during particle

transport. As we will see, the degree to which this stipulation impacts simulation results

will depend on modeling conditions.

   We use two models: the first contains an HEU target, and the second a Pu target. Each

is a small disk (descriptions are given in the following sections). The moving HEU or Pu

target in the respective models is subjected to rectilinear translation at the rate of 880

cm/s. While moving, each target is irradiated by a unidirectional beam of 0.025-eV

neutrons. For each simulation, the neutron beam has a radius that is equal to the target's

radius, and the beam is oriented so that the target moves directly toward the beam. Our

simulated source emits neutrons as a delta function one second after the object begins

moving. In each model the target is surrounded by a vacuum (no other materials are

present in either model) to 1) simplify the time-distance analysis, and 2) avoid issues

associated with neutron transport in media other than the target.

The simulated targets must move a distance for a period of time that is sufficient to

permit delayed-gamma emission during the measurement time windows reported by

Beddingfield and Cecil (1998). So we seek an estimate of the time that the neutrons will

travel in route to the target in order to develop models of adequate size. The Beddingfield

and Cecil experiments involved measurements of the delayed-gamma emission from

approximately 1000 to 1500 s following irradiation. Thus, the moving-objects geometry

must accommodate target motion for approximately 1500 s after fission. This

corresponds to a path length of 1.32d6 cm. Neutrons with energy 0.025 eV have a speed

of approximately 2.322×10^5 cm/s, so the neutrons and target will collide approximately 7

s after the start of the simulation. A more precise estimate can be calculated by solving

the two distance-time-velocity equations for the source and target. But the target's

velocity is small as compared to the neutron velocity, so the less-refined estimate is

sufficient for model development. We thus start each target at $O_z^G = -6.7 \times 10^5$ cm, locate

the source at $O_z^G = +6.7 \times 10^5$ cm (directed in the $-z^G$ direction) , and execute the

calculations for emission and motion time of up to 1500 s in order to accommodate the

time and range of motion and the scoring of delayed-gamma emission events.

Two calculations are executed for each (HEU and Pu) model. These calculations

depict the 1) irradiation of a moving object followed by 2) placement of each target

(individually) in a detector for measurement of the delayed-gamma emission.

The moving-object irradiation calculation for each model is executed by starting a

particle from the source at 1 s. The geometry is updated to its configuration at 1 s, i.e., the

target is moved to its location via rectilinear translation at a constant velocity of 880

cm/s. The target location is frozen at its location at 1 s per Stipulation 4 of Part I

(geometry is fixed during the transport of a source particle). Each source neutron travels

from the source to the target at this location. Prompt particles that are emitted as a result

of the interaction of the source particle with the target (e.g., prompt neutrons, prompt

gammas, etc.) are transported with the target at this location. For each delayed neutron

and gamma, the target is moved to the location corresponding to the time at which each

delayed particle is emitted per Stipulation 4 of Part I (geometry is updated to its

configuration at the time a delayed particle is emitted) .

The selection of the neutron emission time and energy here highlights the moving-

objects limitation regarding the treatment of geometry during particle transport. Clearly,

in reality the source neutrons and object would not interact with the object at its 1-s

location. The opportunity for neutron interaction with the target begins at the time given

by the solution of the coupled distance-time-velocity equations for the source and the

leading edge of the target. The actual time and location of interaction with the target

would depend on the penetration distance of the source particle in the target prior to

interaction. The same can be said for prompt particles emitted as a result of the

interaction of a source particle with the target—the geometry will move during particle

transport. Delayed-particle emission originates with the target located at its 1-s location

rather than the actual physical location. The impact of this limitation is reduced as the

proximity of source and prompt particles to their interaction sites is reduced and the

energies of these particles are increased. For some models, such those used here, the

scored delayed-particle spectra will not be impacted (essentially a Lagrangian detection

scheme will not be affected whereas a Eulerian scheme will be impacted). This limitation

arises from Stipulation 4; capability to treat this limitation lies outside of the scope of the

feature upgrade that we report here.

Now let us return to the simulations at hand. Because we seek to obtain delayed-

gamma spectra with profiles reported for stationary targets (Durkee et al, 2009), the first

calculation requires an arrangement that represents an HPGe detector moving alongside

the target. We model this using the MCNP6 surface-source feature.[†] This feature writes

information (including emission time, energy, direction, location) about the delayed

gammas to a file ("surface source" file). (A special code modification was made in

subroutine **surfac.F**[‡] to store information associated with photons emitted during the

measurement time window). In these calculations, the surface source is located at the

lower surface of the HEU or Pu disk target.

Following the first (irradiation) calculation, the delayed-gamma surface source is

"moved" to our *in silico* HPGe detector to measure the delayed-gamma activity. This

second (measurement) calculation transports the photons from the surface-source to the

detector. The MCNP6 "F8" pulse-height tally is used to simulate the detector response.[*]

[†] The surface-source feature is standard with the general code release. The special modification writes the
     data to the surface-source file only for the stipulated time interval.
[‡] A future upgrade will need to be implemented to treat this without code modification.
[*] The F8 (pulse-height) tally provides the energy distribution of pulses created in a cell that models a
physical detector. The F8 energy bins correspond to the total energy deposited in a detector in the specified
channels by each physical particle (history).

Because the detector design details are not available (Beddingfield and Cecil, 1998),

the physical detector was modeled using the specifications given in Knoll (2000). The F8

tally uses the Gaussian energy broadening ("GEB") special feature ("FT"). The GEB

feature simulates the peak-broadening effects exhibited by physical radiation detectors

using the expression FWHM $= a + b\sqrt{E + cE^2}$, where E is the particle energy. For this

study, the parameters a, b, c were 5.797×10^{-4} MeV, 7.192×10^{-4} MeV$^{1/2}$, 1.0 MeV^{-1} [‡]

(Princeton Gamma Tech, 2006).

Figure 9 illustrates the MCNP6 simulation models for the irradiation and detection

calculations. In the irradiation calculation, the disk-shaped target is moved via rectilinear

translation toward the neutron source. In the detection calculation, the surface source

delayed-gammas are transported in the HPGe detector.

[‡] The simulation used estimated values which should be representative of the Beddingfield and Cecil (1998) detector. The estimates were made using FWHM resolution at 0.122 and 1.33 MeV of 1 and 2 keV, respectively, presuming c=1.
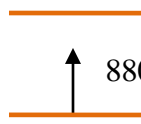
$O_z^G = +6.7 \times 10^5$ cm   Neutron source

Target is moved to the location at the time each delayed gamma is emitted. Delayed gamma information is written to surface source.
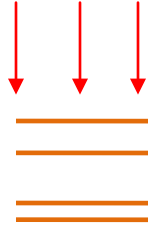
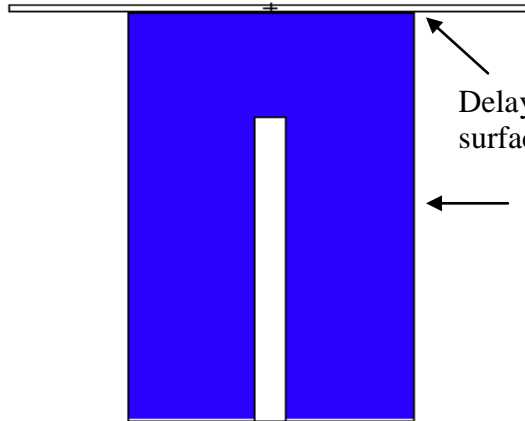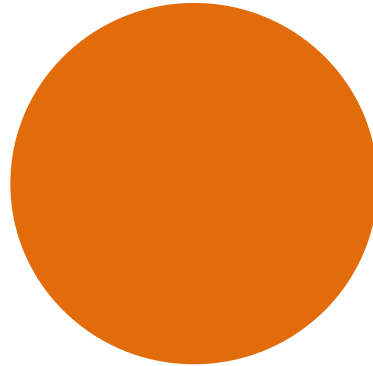Target location at 1 s. Fission and activation occur here.

$O_z^G = -6.7 \times 10^5$ cm

880 cm/s

Disk Target: HEU or Pu

Delayed-particle surface source

HPGe detector

Figure 9. MCNP6 moving target model extending the Beddingfield and Cecil (1998) experimental setup. In the irradiation calculation, a beam source emits 0.025-eV neutrons towards the target to induce fission in the HEU or Pu target. A surface-source file is created for delayed gammas emitted between 1050–1400 s for HEU and 1100–1450 s for Pu after fission. In the measurement calculation, the surface source is read and transported to interact with the HPGe detector (lower image). Detector specs (radius = 1.4 cm, height = 4.50 cm) from Knoll (2000).

Each calculation was run using 200 million source histories.[‡] This quantity of histories

results in reasonable statistics for the F8 pulse-height tallies for the second

(measurement) calculation.[†]

Our hypothesis is that the delayed-gamma emission spectra for the moving and static

HEU and Pu targets should be quite similar. Simulation details are presented next.

2.5.1. Uranium model.

The Beddingfield and Cecil (1998) uranium experiment used a thin disk (5.08-cm

diameter, 0.05588-cm thickness) of material consisting of 93.15 at.% ^{235}U and 6.85 at.%

^{238}U that is irradiated for 100 s irradiation by a moderated ^{252}Cf source. Following

irradiation, the sample was moved to an apparatus where, 1050 s after irradiation, the

delayed-gamma activity was measured for 350 s using an HPGe detector.[†] Our

simulations record the surface source between 1050 and 1400 s following fission.

Figure 10 shows both simulated and experimental results. The lower section of Fig. 10

displays the calculated MCNP6 pulse-height tally obtained using 1-keV resolution (10^4

equal tally bins between 0 and 10 MeV).[*] The upper section of Fig. 10 shows the

---

[‡] In addition, execution was done using analog capture, rather than the default implicit capture, because the F8 pulse-height tally requires analog pulses. Execution also was done with fission and activation. This

[†] The 10 statistical checks provided by MCNP6 for the aggregate (all energy bins) F8 tally are passed. The relative uncertainties for all prominent peaks are < 0.10.

[†] Detector description was not provided by Beddingfield and Cecil (1998) other than to indicate a Princeton Gamma Tech detector.

[*] The MCNP6 "outp" F8 tally data have units of pulses/source particle-MeV. To reflect the measurement time (350 s) and normalize to fissions to obtain units of pulses/fission-s-MeV, the tally data are adjusted using the weight loss for fission (from the first-stage calculation outp file summary table), 0.628 fissions/source particle. This processing was done using MCPLOT commands. The required MCPLOT tally multiplication factor "factor y" value the HEU model is:

measured result (Beddingfield and Cecil, 1998, Fig. 2). The relative uncertainties of the

MCNP6 results are less than 0.10 for the prominent peaks and 0.20 for the low-lying
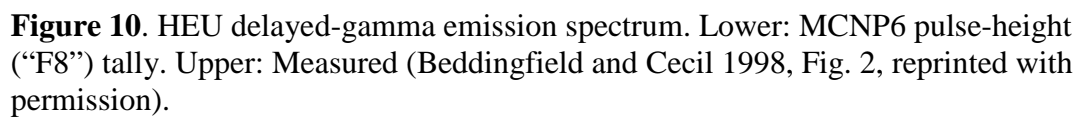
peaks.

Included in Fig. 10 lower are isotopic labels for several of the prominent lines. The

MCNP6 identities of the radiating nuclides for all of the major lines are in agreement

with most of those reported by Beddingfield and Cecil (1998) and Beddingfield (2009).

As was reported for our static models (Durkee et al., 2009), exceptions indicated by the

MCNP6 identification capability are provided in Table 13.[†]

Table 13. Discrepancies between line identification for MCNP6 and measured data

(Beddingfield and Cecil, 1998).

MCNP6		Measured	
Gamma Energy (MeV)	Emitting Nuclide(s)	Gamma Energy (MeV)	Emitting Nuclide(s)
0.8394	^{130}Sb+^{130m}Sb	0.8317	^{90}Rb+^{90m}Rb
0.8470	^{134}I	0.8394	^{130}Sb+^{130m}Sb
0.8840, 0.8844	^{134}I+^{104}Tc	0.8882	^{93}Sr
1.4359	^{138}Cs	1.4276	^{94}Sr
1.5247	^{146}Pr	1.5325	^{101}Mo
1.5325	^{101}Mo	unlabelled	unlabelled

---

factor =f1photons/src part-MeV*1/((1400-1050)s*6.28d-1fiss/src part))=4.55e-3 pulses/fiss-s-MeV
This factor was then incorporated into MCPLOT commands for the HEU simulation using the following
command sequence:
tal 858 noerr linlin xlims 0.8 1.55 ylims 0 0.00004 legend 1.35 3.5e-5
fixed t=2 factor y 4.55e-3 label "1050-1400s"

[†] In Durkee et al., 2009, the nuclides ^{130}Sb+^{130m}Sb were reported with typo errors as ^{131}Sb+^{131m}Sb. Also,
    after further review, we concur that the first line above the ^{89}Rb 1.2481 MeV line is the 1.2604 MeV
    emission by ^{135}I. The ^{101}Mo emission at 1.2511 MeV contributes to the higher-energy portion of
    structure of the prominent peak that is labeled as ^{89}Rb.

Figure 10. HEU delayed-gamma emission spectrum. Lower: MCNP6 pulse-height ("F8") tally. Upper: Measured (Beddingfield and Cecil 1998, Fig. 2, reprinted with permission).

This agreement of simulated and measured values supports our hypothesis. The HEU *in silico* emission spectrum closely resembles the profile obtained by measurement and as well as the result we reported for the static configuration (Durkee et al., 2009).

To help illustrate delayed-gamma emission from the moving target, we show simulation results obtained using the MCNP6 mesh tally of the photon flux.[†] Figure 11 shows a mesh tally of prompt gammas flux, while Fig. 12 the prompt and delayed gammas.[‡] The structure of the photon field in these plots is similar at early times, or axial locations less than -2×10^5 cm. At later times, or axial locations greater than -2×10^5 cm, the prompt-gamma field in Fig. 11 has a spherical shape. These photons are emitted with the target 880 cm above its initial position. The prompt+delayed field in Fig. 12 is non-spherical above -2×10^5 cm because the target is moved to the location corresponding to the time at which each delayed-gamma is emitted. Increased photon emission occurs along the axis along which the target moves.

[†] The MCNP6 mesh tally displays the particle flux on a rectangular grid overlaid atop the problem geometry.

[‡] Separate calculation using the same input deck with no phys:p card, which causes only prompt-gamma treatment.
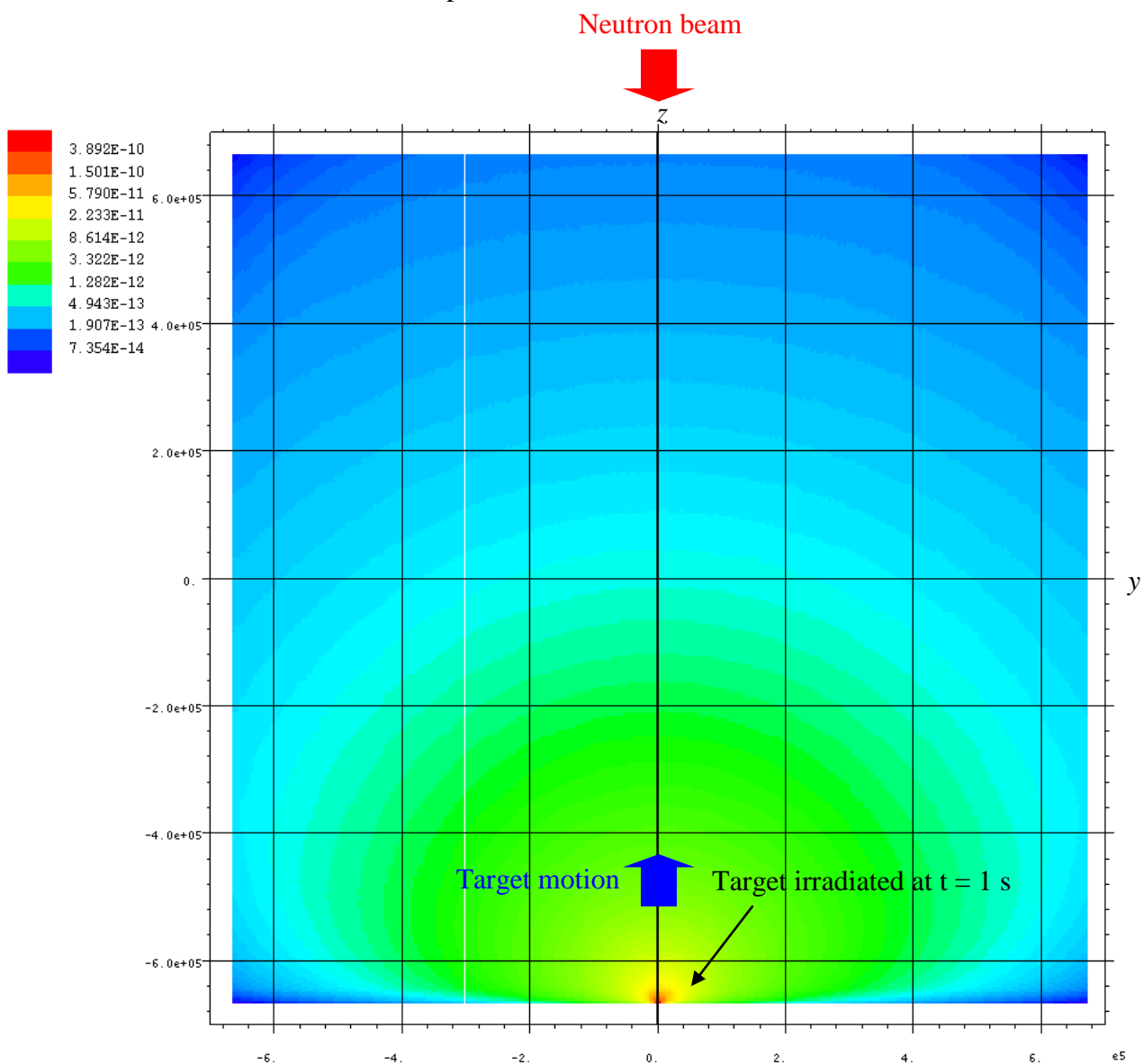
Figure 11. Mesh tally (photons/cm^2-source neutron) of prompt-gamma emission from the moving HEU target (axes in cm).
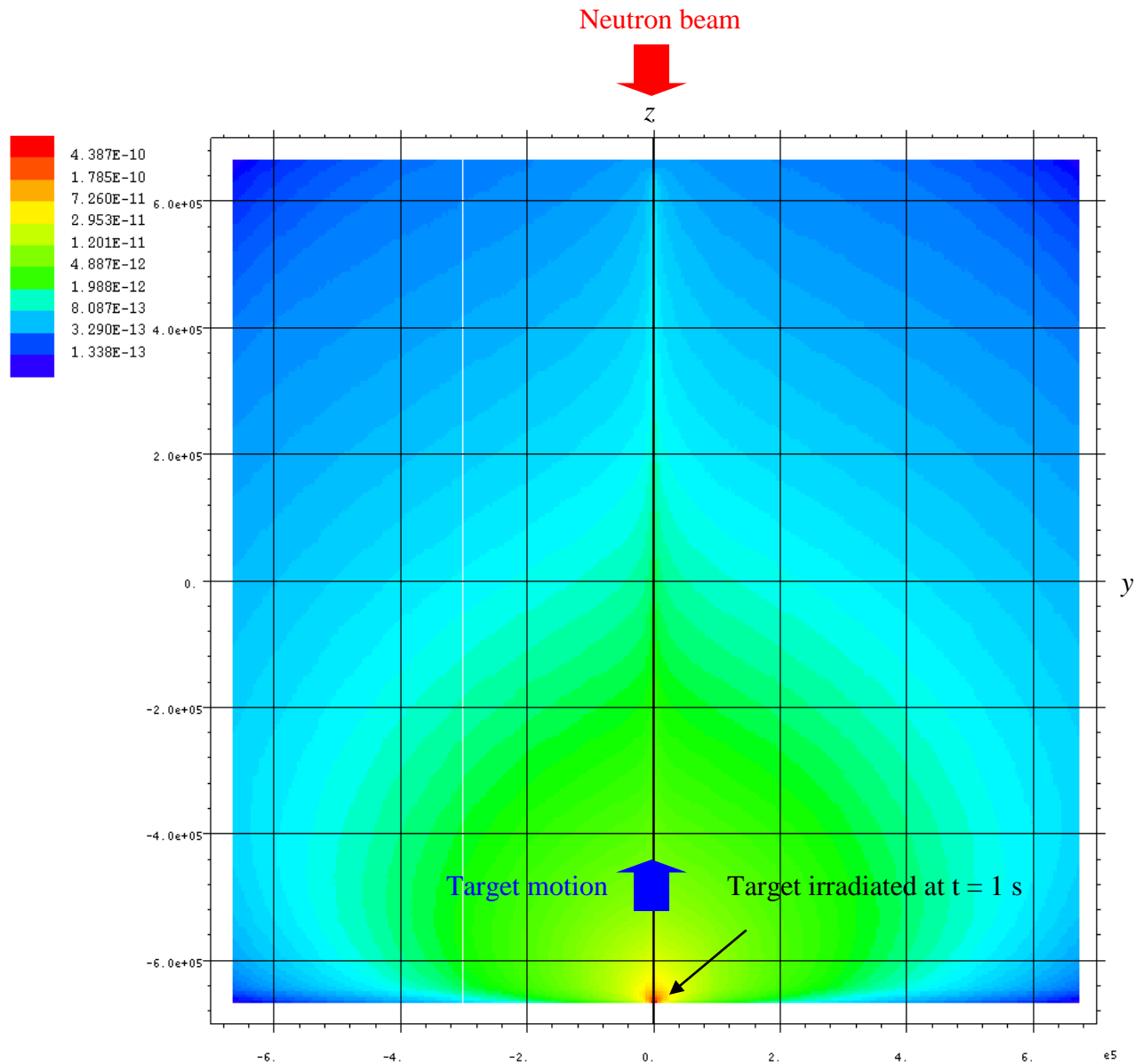
Figure 12. Mesh tally (photons/cm^2-source neutron) of prompt- and delayed-gamma emission from the moving HEU target (axes in cm).

Figures 13 and 14 show only delayed-gamma fields.[*] Figure 13 shows only delayed gammas emitted 7.5 s or later. The source neutrons are emitted at 1 s and require approximated 6.2 s to reach the target. Thus, the resulting photon field is comprised of the bulk of the delayed-gammas. Pronounced emission occurs at early times, or axial

---

[*] These figures were produced by simulations with the mesh tally windowed in time.

locations less than -6×10^5 cm. Figure 14 shows only delayed gammas emitted within the

Beddingfield measurement time window between 1050 and 1400 s, or between axial

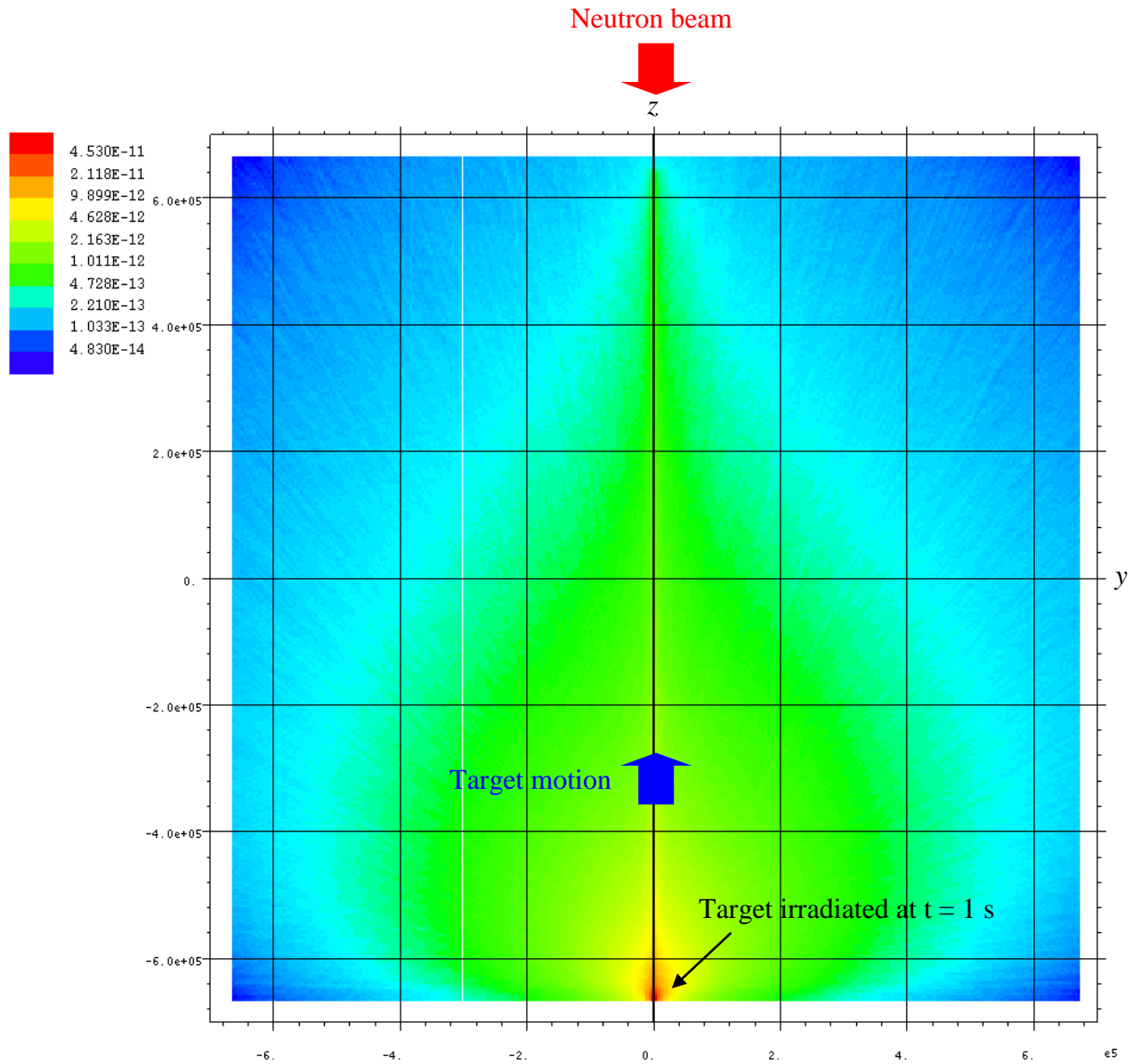locations approximately 2.5×10^5 and 5.5×10^5 cm.

Figure 13. Mesh tally (photons/cm^2-source neutron) of delayed-gamma emission from the moving HEU target at 7.5 s or later (axes in cm).
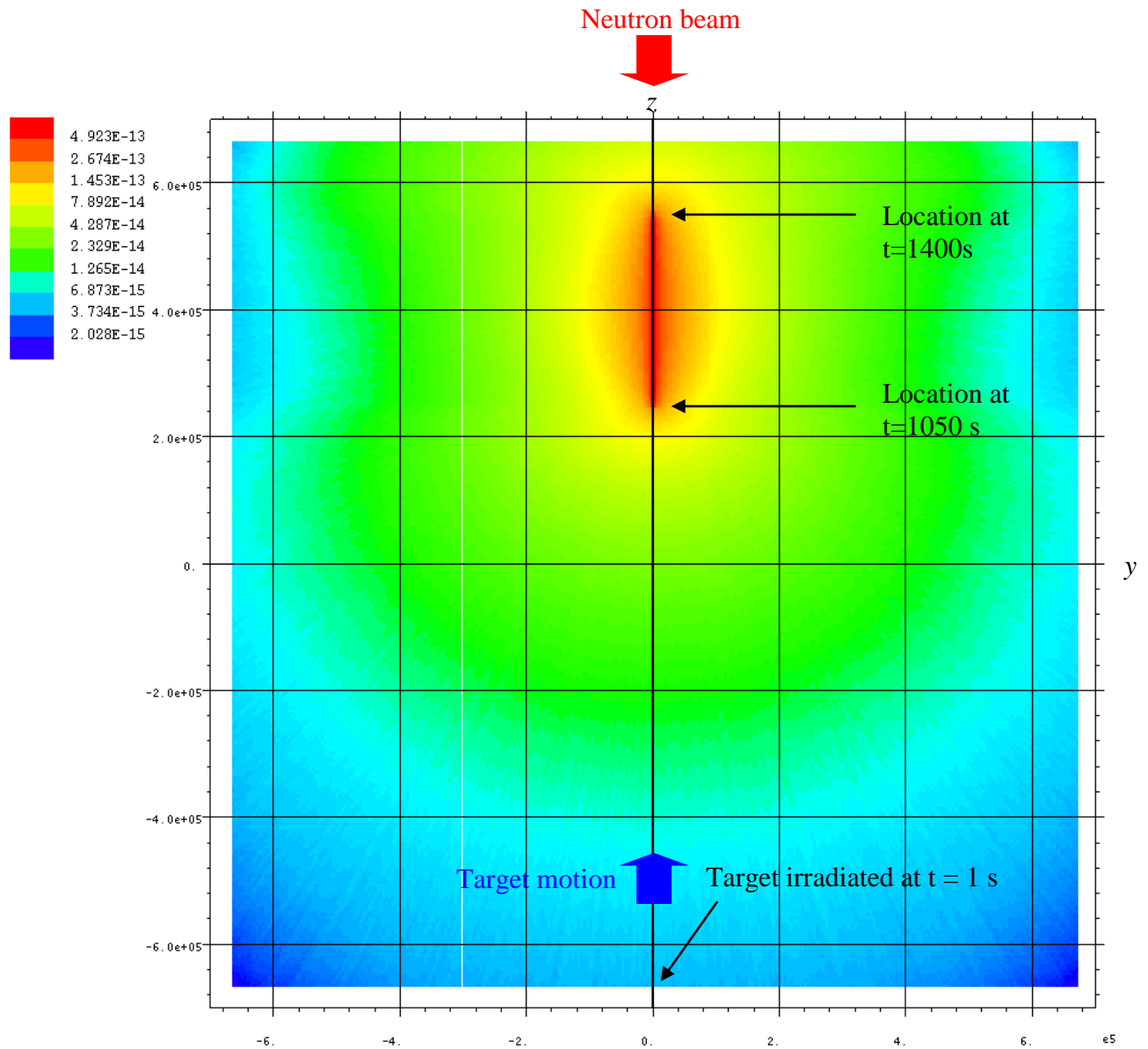
Figure 14. Mesh tally (photons/cm^2-source neutron) of delayed-gamma emission between 1050 and 1400 s following fission from moving HEU target (axes in cm).

The images in Figs.11–14 are the aggregates of many photon tracks. The image in

Fig.15 shows individual delayed-gamma tracks emitted between 1050 and 1400 s for

execution using only 1000 source-neutron histories. The photons are emitted isotropically

from the HEU target located at its positions corresponding to the times at which each
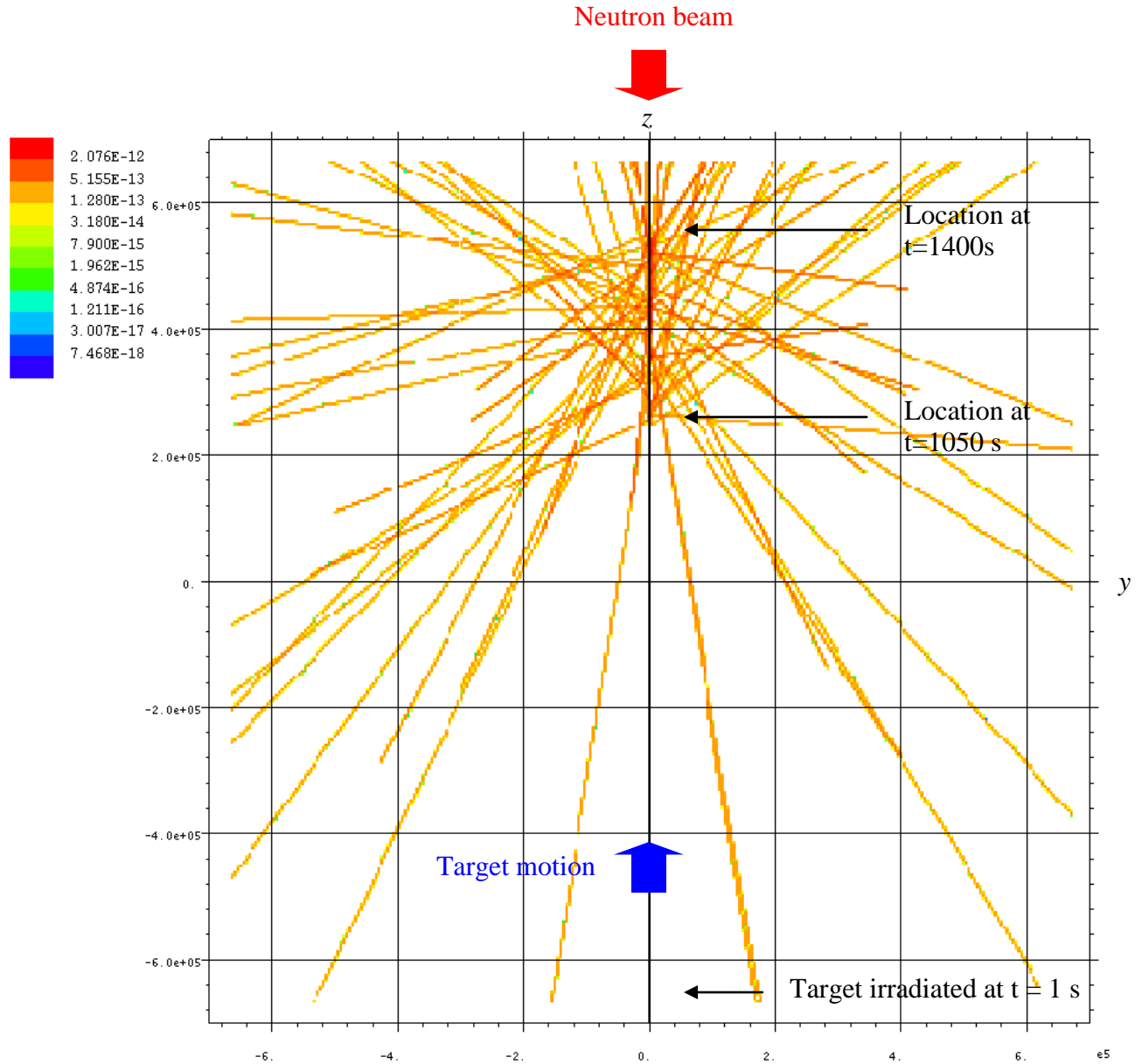
delayed-gamma is emitted. [†]

Figure 15. Mesh tally (photons/cm^2-source neutron) of delayed-gamma emission from the
moving HEU target between 1050 and 1400 s (axes in cm) for 1000 source-neutron histories.

[†] A single *x*-mesh zone was used in the direction orthogonal to the plane of the image. Some of the particle
  tracks end within the mesh because they exit mesh either into and out of the *x*-mesh zone.

Additionally, this analysis and its comparison to experiment provides an initial pseudo-validation of the moving-objects feature. This simulation required the use of many of the upgrade's facets to facilatate the calculation, including new input processing, new geometry-modification algorithms, handling of prompt and delayed particles inclusive of operations involving the bank, and MPI upgrades needed to treat moving objects. Importantly, no particles were lost during execution.

The HEU irradiation calculation (during which the surface-source was generated) required 73 hr 12 2.4-GHz quad-processor nodes on a Linux cluster, while the measurement calculation (which evaluated the HPGe detector response to the surface source gammas) required a few seconds to execute on a PC. The executable was made using the Portland Group FORTRAN 90 compiler, and an MPI build. For comparison purposes, execution of our static HEU model (Durkee et al., 2011) using this executable and the same execution platform and configuration required 34 hr of CPU time.

2.5.2. Plutonium model.

The Beddingfield and Cecil (1998) plutonium experiment closely resembles the uranium experiment. The plutonium disk (5.08-cm diameter, 0.05588-cm thickness) consisted of 98.97 at. % ^{239}Pu, 0.58 at. % ^{240}Pu,   0.0335 at. % ^{241}Pu, 0.0179 at. % ^{242}Pu, and was clad with 0.0508 cm of copper. The sample was irradiated for 100 s using a moderated ^{252}Cf source. Following irradiation, 1100 s elapsed as the sample was moved to an HPGe detector. Subsequently, photon data was acquired over a period of 350 s.

Our MCNP6 model recorded delayed gammas emitted between 1100 and 1450 s

following fission.

Figure 16 lower contains the calculated pulse-height tally obtained using 1-keV

resolution (10^4 equal tally bins between 0 and 10 MeV). [†] The upper section of Fig. 16

shows the measured result (Beddingfield and Cecil 1998, Fig. 2). Relative uncertainties

for the prominent peaks are less than 0.10 and for the low-lying peaks are less than 0.20.

The simulated spectra is in good agreement with the experimental data, with the same

peak identification exceptions as noted for the HEU simulation.

[†] The MCNP6 "outp" file summary table indicates 0.582 fissions/source particle for the plutonium model simulation. The required MCPLOT tally multiplication factor "factor y" value for the plutonium model is given by:
factor =f1photons/src part-MeV*1/((1450-1110)s*5.82d-1fiss/src part))=4.90e-3 pulses/fiss-s-MeV
This factor was then incorporated into MCPLOT commands for the plutonium simulation using the following command sequence:
tal 858 noerr linlin xlims 0.8 1.55 ylims 0 0.000045 legend 1.35 3.8e-5
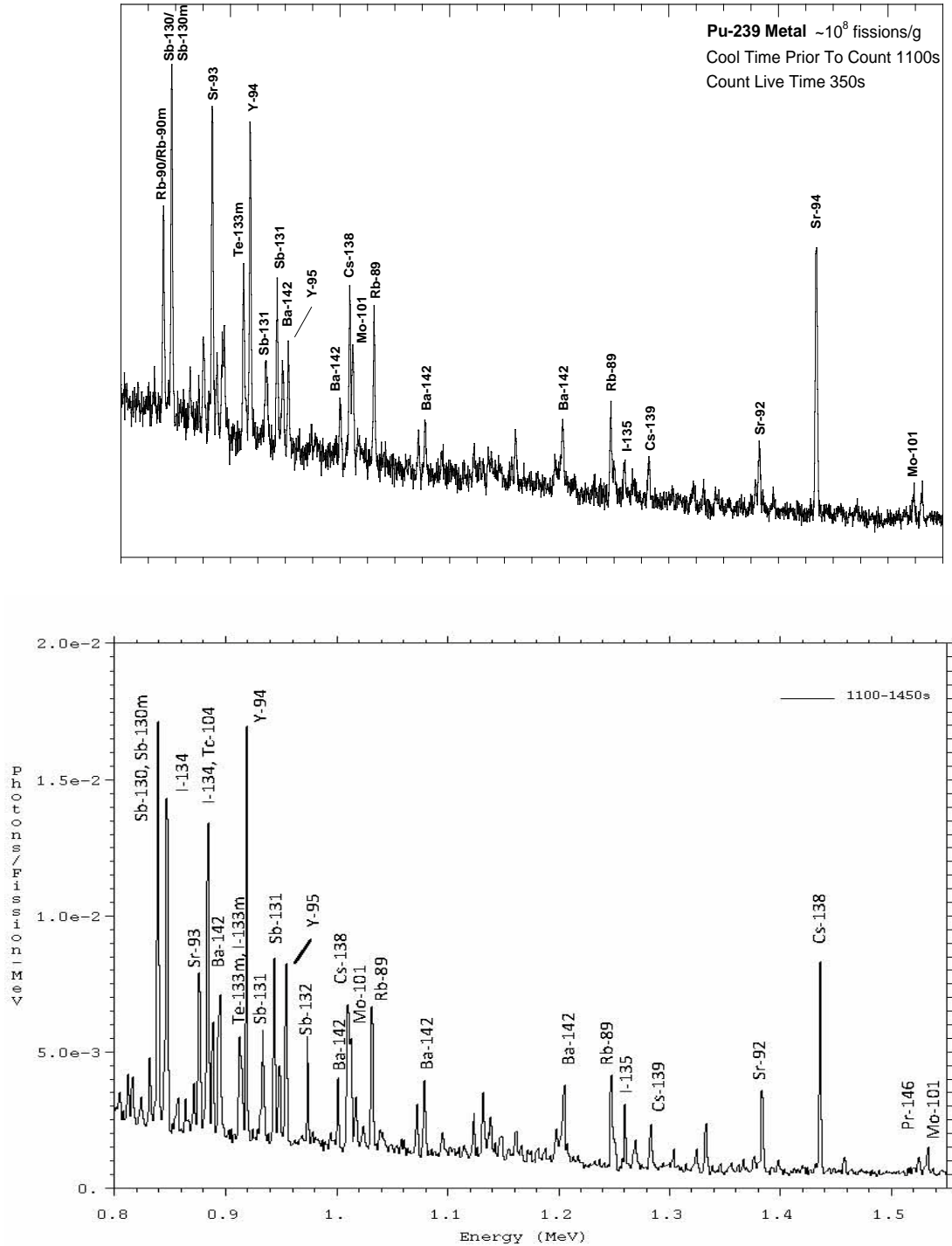fixed t=2 factor y 4.90e-3 label "1100-1450s"

Figure 16. Plutonium delayed-gamma emission spectrum. Lower: MCNP6 pulse-height ("F8") tally. Upper: Measured (Beddingfield and Cecil, 1998, Fig. 2, reprinted with permission).

This result substantiates our hypothesis. As was the case for HEU, the simulated Pu emission spectrum closely resembles the measured profile. This simulation, which executed with no lost particles, also helps to validate the moving-objects feature.

Figures 17 shows a mesh tally of prompt gammas flux, while Fig. 18 the prompt and delayed gammas. The structure of the photon field in these plots is similar at early times, or axial locations less than -2×10^5 cm. At later times, or axial locations greater than -2×10^5 cm, the prompt-gamma field in Fig. 17 has a spherical shape. These photons are emitted with the target 880 cm above its initial position. The prompt+delayed field in Fig. 18 is non-spherical above -2×10^5 cm because the target is moved to the location corresponding to the time at which each delayed-gamma is emitted. Increased photon emission occurs along the axis along which the target moves.
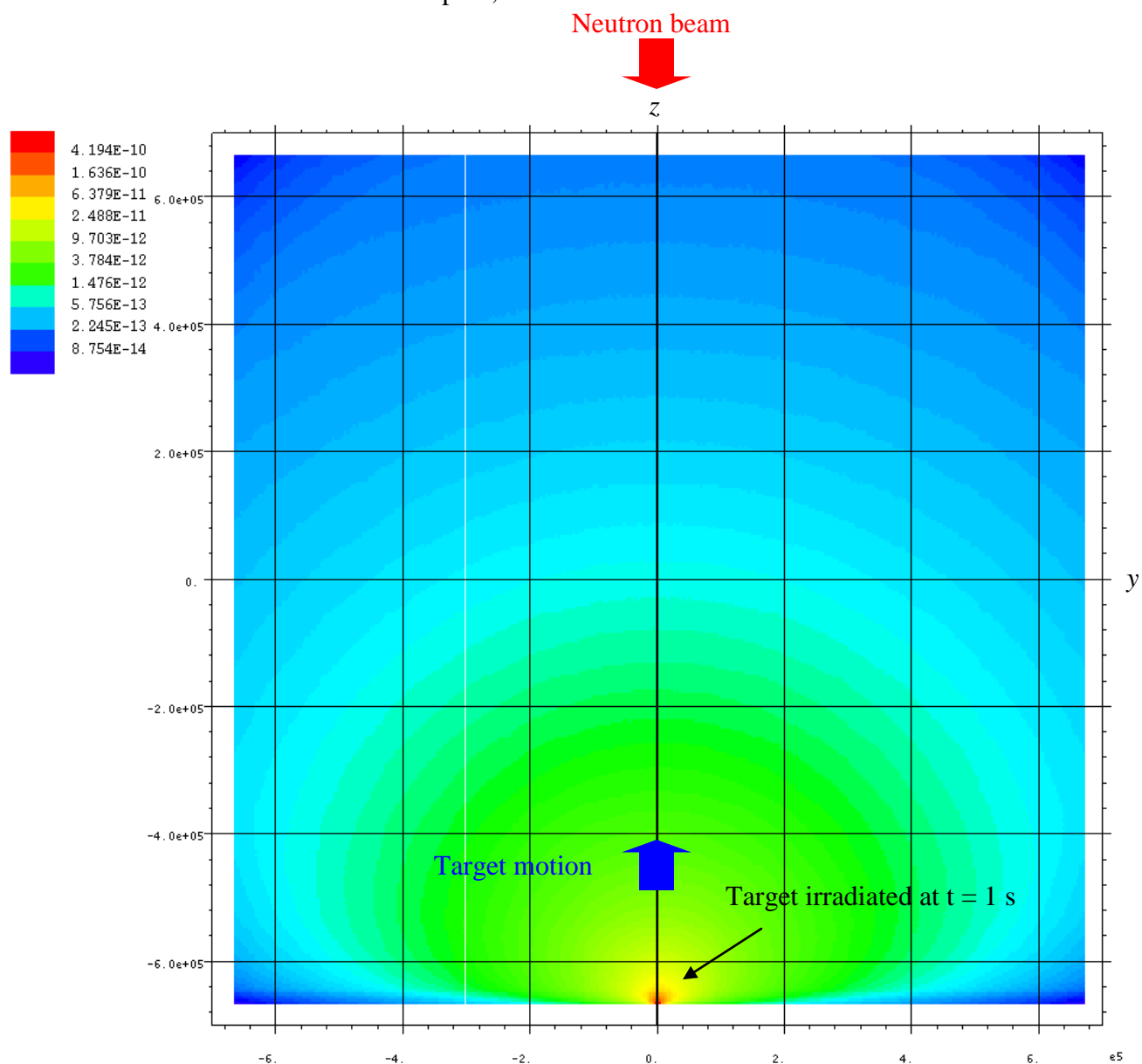
Figure 17. Mesh tally (photons/cm^2-source neutron) of prompt-gamma emission from the moving plutonium target (axes in cm).
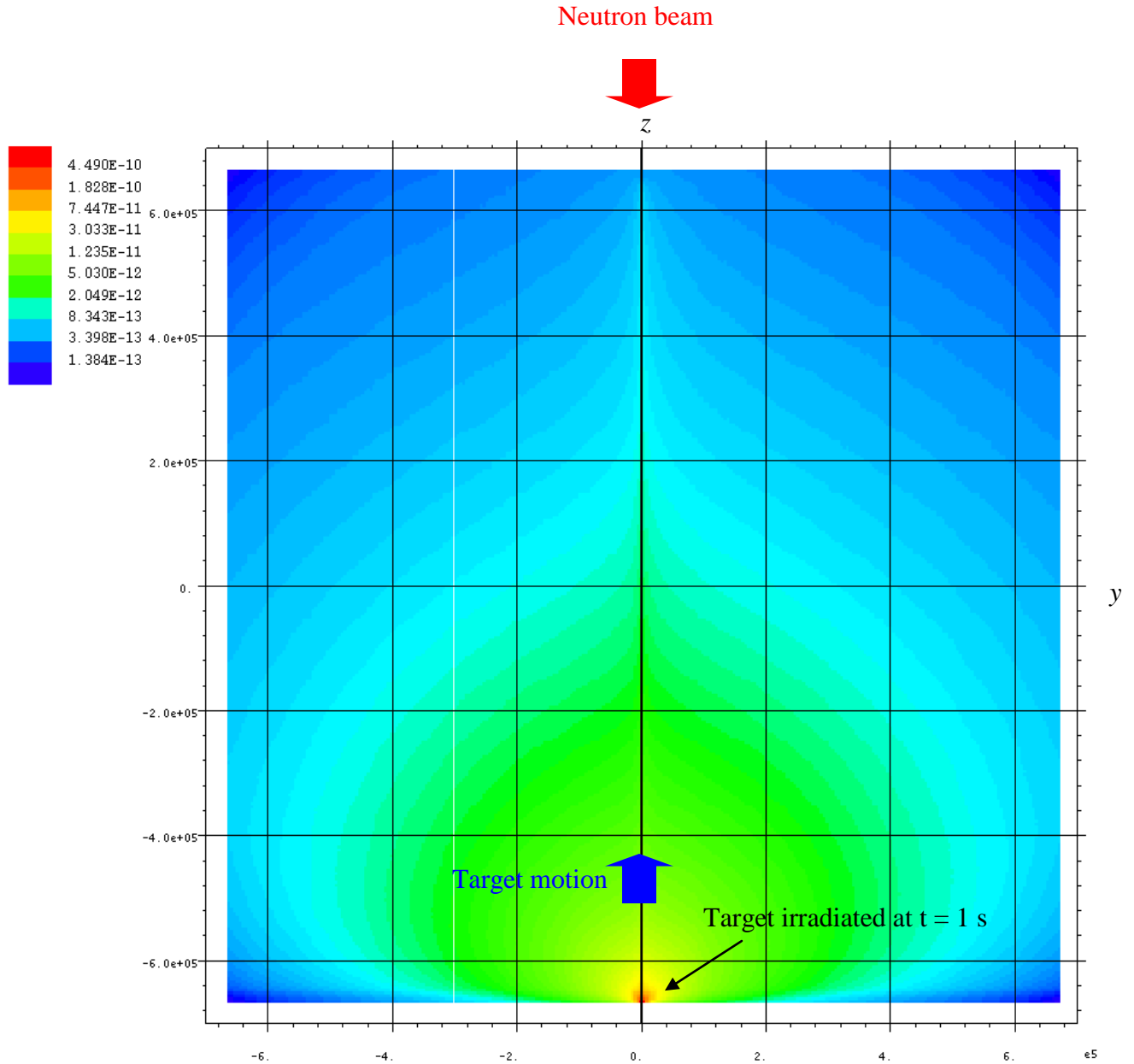
Figure 18. Mesh tally (photons/cm^2-source neutron) of prompt- and delayed-gamma emission from the moving plutonium target (axes in cm).

Figures 19 and 20 show only delayed-gamma fields. Figure 19 shows only delayed gammas emitted 7.5 s or later. Pronounced emission occurs at early times, or axial locations less than -6×10^5 cm. Figure 20 shows only delayed gammas emitted within the

Beddingfield measurement time window between 1100 and 1450 s, or between axial

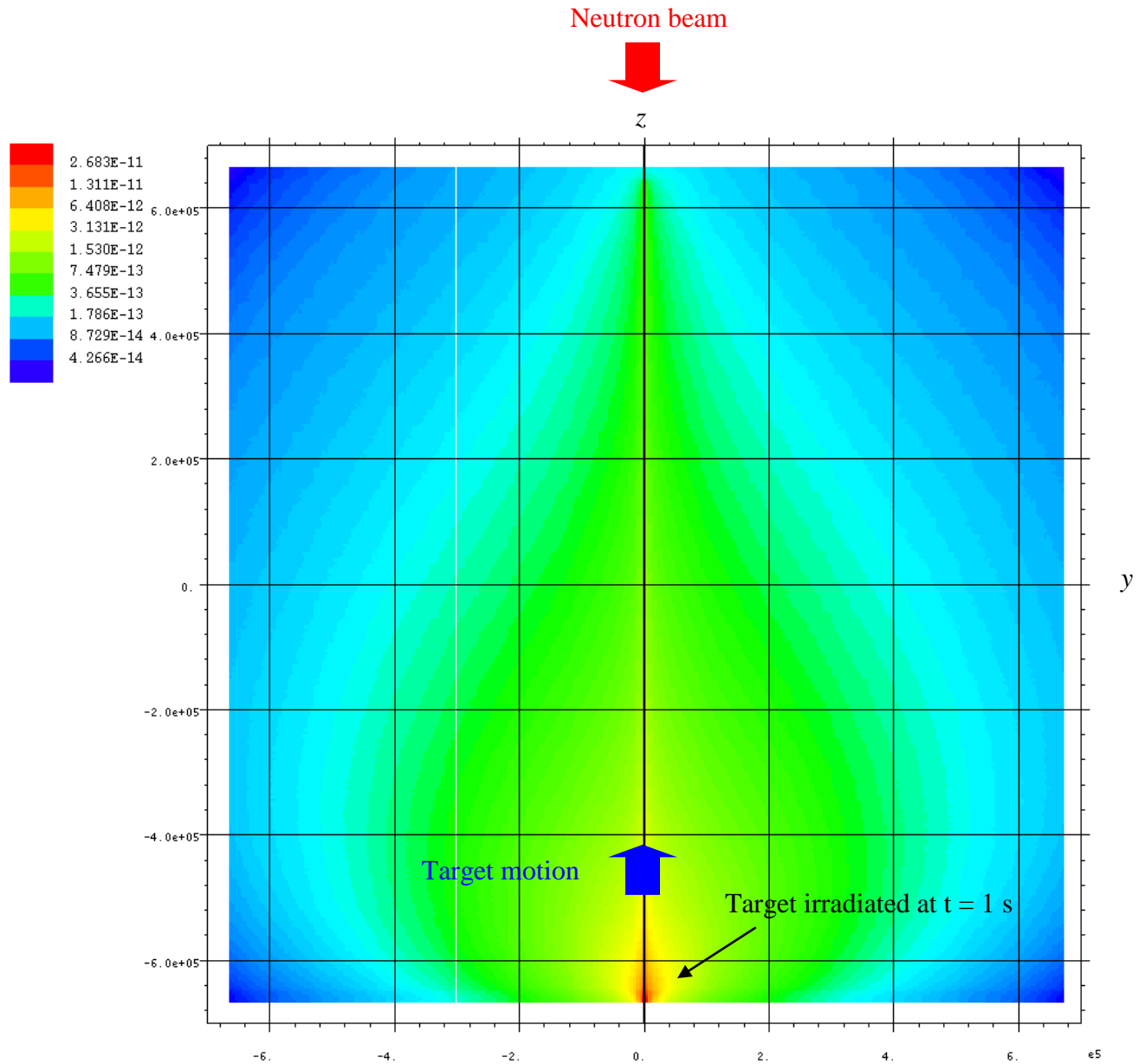locations approximately 2.5×10^5 and 5.5×10^5 cm.

Figure 19. Mesh tally (photons/cm^2-source neutron) of delayed-gamma emission from the moving plutonium target at 7.5 s or later (axes in cm).
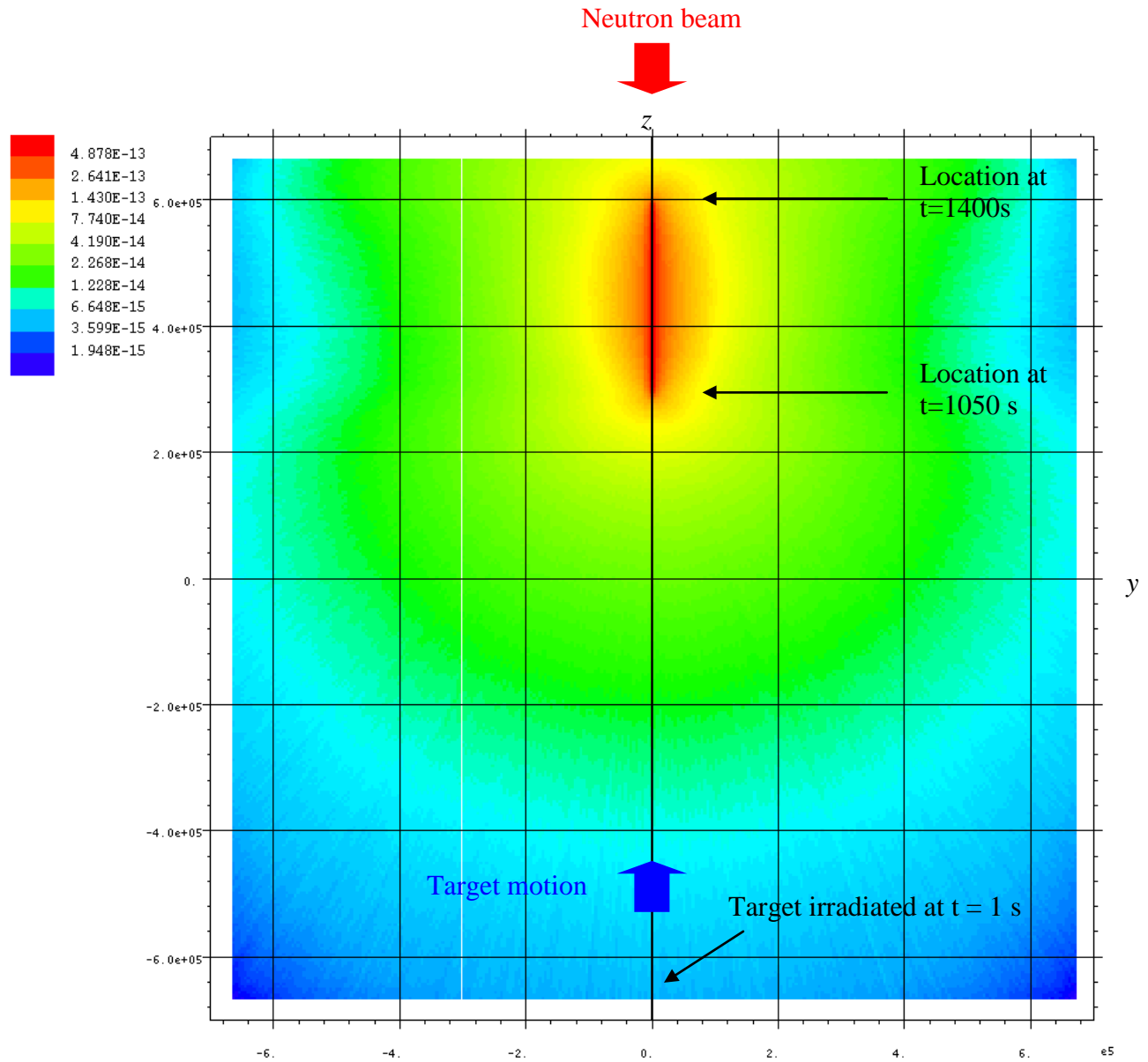
Figure 20. Mesh tally (photons/cm^2-source neutron) of delayed-gamma emission between 1050 and 1400 s following fission from moving plutonium target (axes in cm).

The Pu irradiation calculation required 83 of CPU time using 12 2.4-GHz quad-processor nodes on a Linux cluster, while the measurement calculation required a few seconds to execute on a PC. The executable was made using the Portland Group FORTRAN 90 compiler and an MPI build. For comparison purposes, execution of our

static Pu model (Durkee et al., 2011) using this executable and the same execution platform and configuration required 36 hr of CPU time.

3.   Summary and conclusions

Extensive upgrades have been made to MCNP6 to enable radiation-transport simulations involving object, source, and delayed-particle motion. In Part I we detailed the dynamics equations that have been implemented in MCNP6 for rectilinear and curvilinear motion. We also described upgrades to the MCNP6 plotg utility that permit the viewing of time-evolving geometry.

In Part II we have demonstrated the moving-objects capability using several models. The first set of models depicts several types of object motion. Included are numerous plots of the time-evolving geometry created using the plotg utility and its new "time" command. The simulations demonstrate functionality of movement involving rectilinear translation, curvilinear translation, and curvilinear rotation motion segments. In addition, linking of individual motion segments to form more complicated paths was demonstrated.

The second set of models were related to the Beddingfield and Cecil (1998) HEU and Pu experiments involving delayed-gamma spectra. In our simulations, the HEU and Pu targets were moved via rectilinear translation in a vacuum and exposed to a beam of 0.025 eV neutrons. After the target irradiation calculation was complete, the *in silico* irradiated targets were moved to a simulated HPGe detector. The simulated delayed-gamma emission spectra agrees well with the data reported by Beddingfield and Cecil.

Although the results from these two sets of models are promising, our verification and validation efforts for the moving-objects feature are in their infancy. We anticipate additional future efforts in this regard. These simulations used nearly all of the upgrade's facets, including new input processing, new geometry-modification algorithms, handling of prompt and delayed particles inclusive of operations involving the bank, MPI upgrades that were needed to treat moving objects, and plotg upgrades for time-dependent plots of the geometry.

It is important to note that the simulations involving particle creation and transport generated no lost particles and the plots displayed without any anamolies. Prior to the moving-objects feature, lost particles typically were indicative of user-induced geometry errors in an input file, and plot anamolies were exceedingly rare. During the development of the moving-objects feature, lost particles were observed for various models, and bona fide plot anamolies were seen for models that involved curvilinear rotation. The resolution of several theoretical and code-development issues culminated in a feature that appears to properly handle the particles and geometry within the scope of the Stipulations listed in Part I.

As expected, the geometry updates cause simulations involving object motion to require more time to execute than similar models involving only static objects. Simulations that specify only object translation execute more quickly than those that require translation and rotation. This increase occurs because of the need to solve a

system of equations for the time-dependent object orientation when rotation is involved.

The increase in simulation time also depends on the modeling needs and associated

statistics. For example, calculations specifying a series of stepwise movements will likely

require less execution time to produce adequate statistical results than simulations that

model continuous motion.

The moving-objects feature should find a wide assortment of applications within

Monte Carlo radiation transport community. For example, this feature negates the need to

execute a series of quasi-static calculations using scripts. Instead, self-contained

simulations can be conducted using object motion. Applications areas could include

initiatives in homeland security, biomedicine, nuclear-reactor design and analysis,

radiological safety, oil-well logging, radiation exposure in space, and many more.

Acknowledgements

Support for this work has been provided by the Department of Homeland Security Domestic Nuclear Detection Office. We appreciate David Beddingfield providing the figures depicting experimental data.

References

Beddingfield D.H, 2009. Private communication.

Beddingfield D.H. and Cecil F.E., 1998. "Identification of Fissile Materials From Fission Product Gamma-Ray Spectra," Nuclear Instruments and Methods in Physics Research A; v.417, pp. 405–412.

Durkee Joe W., Jr., McKinney Gregg W., Trellue Holly R., Waters Laurie S., and Wilson W.B., 2009. "Delayed-Gamma Simulation Using MCNPX. Part II: Simulations," Progress in Nuclear Energy, **51**, 828-836.

Durkee Joe W., Jr., James Michael R., McKinney Gregg W., Waters Laurie S., and Goorley Tim, 2011. "The MCNP6 Delayed-Particle Feature," in preparation for J. of Nuclear Technology.

Goorley T., James M., Booth T., Brown F., Bull J., Cox L.J., Durkee J., Elson J., Fensin M., Forster R.A., Hendricks J., Hughes H.G., Johns R., Kiedrowski B., Martz R., Mashnik S., McKinney G., Pelowitz D., Prael R., Sweezy J., Waters L., Wilcox T., and Zukaitis T., "Initial MCNP6 Release Overview," *J. Nuclear Technology*, submitted December 2011.

Knoll G.F., 2000. *Radiation Detection and Measurement*, John Wiley & Sons, Inc., New York, pp. 406–415.

Pelowitz D.B., ed., April 2008. "MCNPX User's Manual Version 2.6.0," Los Alamos National Laboratory report LA-CP-07-1473.

Princeton Gamma Tech, 2006. website http://www.pgt.com/Nuclear/IGC_specs.html.

APPENDIX

For an object that is moving along a path that is not parallel to either the $x^G - y^G$,

$x^G - z^G$, or $y^G - z^G$ MCNP6 global-coordinate planes, the creation of the geometry for

input into MCNP6 is somewhat challenging. The difficulty occurs even though the path-

coordinate specifications are readily specified (i.e., the axis-of-rotation, radius-of-

curvature, angular speed and acceleration). However, obtaining the cosines of the angles

between the global and path-coordinate axes, the $B_1^{GP} - B_9^{GP}$, where

$$
\begin{aligned}
B_1^{GP} &= \hat{i}^P \cdot \hat{i}^G, & B_2^{GP} &= \hat{j}^P \cdot \hat{i}^G, & B_3^{GP} &= \hat{k}^P \cdot \hat{i}^G \\
B_4^{GP} &= \hat{i}^P \cdot \hat{j}^G, & B_5^{GP} &= \hat{j}^P \cdot \hat{j}^G, & B_6^{GP} &= \hat{k}^P \cdot \hat{j}^G \\
B_7^{GP} &= \hat{i}^P \cdot \hat{k}^G, & B_8^{GP} &= \hat{j}^P \cdot \hat{k}^G, & B_9^{GP} &= \hat{k}^P \cdot \hat{k}^G
\end{aligned}
\tag{1}
$$

is not a trivial task because the components of the path's orientation along the axes x^P, y^P,

and z^P must be specified. This difficulty is not unique to the path coordinates used for the

new moving-objects feature—the same issue arises for the long-standing MCNP6 feature

involving the orientation of an object using $B_1^{GL} - B_9^{GL}$.

We present here one approach for systematically creating a moving-objects model that

travels a circular path selected to be in a plane that intersects the global-coordinate axes

at the points a^G, b^G and c^G. The object is designated to move in the counterclockwise

direction along the path starting from the x^P axis. The formulation here pertains to Test

Model 3 as illustrated in Fig. 4. In the following discussion, we derive the expressions for

the location and orientation of the path: O_{Ax}^G, O_{Ay}^G, O_{Az}^G, and $B_1^{GP} - B_9^{GP}$ given a^G, b^G and

c^G. These values are needed for input into MCNP6.

First we calculate a vector normal to the plane. Vectors from point a^G to b^G and from

b^G to c^G are

$$\vec{V}_{ab} = b^G \hat{j}^G - a^G \hat{i}^G \tag{2}$$

and

$$\vec{V}_{bc} = c^G \hat{k}^G - b^G \hat{j}^G . \tag{3}$$

A vector normal to the plane is calculated by taking the cross product of these two

vectors:

$$\vec{N}^G = \vec{V}_{ab} \times \vec{V}_{bc} = b^G c^G \hat{i}^G + a^G c^G \hat{j}^G + a^G b^G \hat{k}^G . \tag{4}$$

Later we will need to use the unit vector $\hat{n}^G$, which is given by

$$\hat{n}^G = \frac{\vec{N}^G}{|\vec{N}^G|} = n_i^G \hat{i}^G + n_j^G \hat{j}^G + n_k^G \hat{k}^G \frac{b^G c^G \hat{i}^G + a^G c^G \hat{j}^G + a^G b^G \hat{k}^G}{\left(b^G c^G\right)^2 + \left(a^G c^G\right)^2 + \left(a^G b^G\right)^2} . \tag{5}$$

The equation of the plane is given by the dot product of a vector normal to the plane and

a vector in the plane

$$\vec{N}^G \cdot \left(\bar{O}^G - \vec{P}_0^G\right) = 0 , \tag{6}$$

where

$$\bar{O}^G = O_x^G \hat{i}^G + O_y^G \hat{j}^G + O_z^G \hat{k}^G \tag{7}$$

is the location of the object at the start of the motion segment and

$$\vec{P}_0^G = x_0^G \hat{i}^G + y_0^G \hat{j}^G + z_0^G \hat{k}^G \tag{8}$$

is a vector from the MCNP6 global coordinate origin to the point $\left(x_0^G, y_0^G, z_0^G \right)$.

Selecting the point $x_0^G = a^G$, $y_0^G = 0$, $z_0^G = 0$ as the point in the plane and plugging these

values into Eq.(6) gives the equation of the plane through points a^G, b^G and c^G

$$b^G c^G O_x^G + a^G c^G O_y^G + a^G b^G O_z^G - a^G b^G c^G = 0 \,. \tag{9}$$

The location of the axis-of-rotation O_{Ax}^G, O_{Ay}^G, O_{Az}^G can be stipulated by picking values

for O_{Ax}^G and O_{Ay}^G, plugging them into Eq.(9), and solving for O_{Az}^G to give

$$O_{Az}^G = \frac{a^G b^G c^G - \left(b^G c^G O_{Ax}^G + a^G c^G O_{Ay}^G \right)}{a^G b^G} \,. \tag{10}$$

Next we determine a vector $\bar{B}^G$ in the direction of the path x^P axis from $\bar{O}_A^G$ to b^G

$$\bar{B}^G = b^G \hat{j}^G - \bar{O}_A^G \,, \tag{11}$$

which we write as

$$\bar{B}^G = a_{\bar{x}}^G \hat{i}^G + b_{\bar{x}}^G \hat{j}^G + c_{\bar{x}}^G \hat{k}^G \,, \tag{12}$$

where

$$a_{\bar{x}}^G = -O_{Ax}^G, \quad b_{\bar{x}}^G = b^G - O_{Ay}^G, \quad c_{\bar{x}}^G = -O_{Az}^G \,. \tag{13}$$

The corresponding unit vector $\hat{b}^G$ is $\bar{B}^G$ divided by its magnitude,

$$\hat{b}^G = \frac{\bar{B}^G}{\left| \bar{B}^G \right|} = b_i^G \hat{i}^G + b_j^G \hat{j}^G + b_k^G \hat{k}^G \,. \tag{14}$$

We now find $\bar{O}^G$, the location of the object at time $t = 0$, where $\hat{b}^G$ intersects the

circular path at radius ρ. To do so, we use the parametric form of the equation of a line

through $\bar{O}_A^G$ in the direction $\bar{B}^G$. In terms of the parameter s we have

$$O_x^G = O_{Ax}^G + a_{\bar{x}}^G s$$
$$O_y^G = O_{Ay}^G + b_{\bar{x}}^G s \;. \tag{15}$$
$$O_z^G = O_{Az}^G + c_{\bar{x}}^G s$$

The radius of curvature is

$$\rho = \left| \bar{O}^G - \bar{O}_A^G \right| \tag{16}$$

so that setting $s = s_{POI}$ in Eq.(15) and solving for s_{POI} gives

$$s_{POI} = \rho \left(a_{\bar{x}}^{G2} + b_{\bar{x}}^{G2} + c_{\bar{x}}^{G2} \right)^{-1/2} . \tag{17}$$

Using Eq.(17) in Eq.(15) gives the starting location of the object on the path.

The $B_\xi^{GP}, \xi = 1, \ldots, 9$ now can be calculated. From Eq.(1), we need the unit vectors

$\hat{i}^P, \hat{j}^P$, and $\hat{k}^P$ that are directed along the path coordinate axes. For $B_1^{GP} - B_3^{GP}$, we note

that $\hat{b}^G$ is parallel to $\hat{i}^P$. Recalling the vector cross product expression

$$\left| \bar{A} \times \bar{B} \right| = \left| \bar{A} \right| \left| \bar{B} \right| \sin \theta , \tag{18}$$

we can calculate θ_ξ by taking the cross product of $\hat{i}^G, \hat{j}^G$, and $\hat{k}^G$ and $\hat{b}^G$ to give

$$\theta_\xi = \sin^{-1} \left(\frac{\left| \bar{A} \times \hat{b}^G \right|}{\left| \bar{A} \right| \left| \hat{b}^G \right|} \right), \xi = 1, 2, 3 , \tag{19}$$

where $\bar{A} = \hat{i}^G, \hat{j}^G, \hat{k}^G$ for $\xi = 1, 2, 3$, respectively. Thus, for $B_1^{GP} = \hat{i}^G \cdot \hat{i}^P = \cos \theta_1$

$$\hat{i}^G \times \hat{b}^G = b^G \hat{k}^G - c^G \hat{j}^G$$
$$\left| \hat{i}^G \times \hat{b}^G \right| = \left(b_{\bar{x}}^{G2} + c_{\bar{x}}^{G2} \right)^{1/2} / \left| \bar{B}^G \right| \tag{20}$$
$$\left| \hat{i}^G \right| = \left| \bar{b}^G \right| = 1 \quad ,$$

so that

$$\theta_1 = \sin^{-1}\left[\left(b_{\bar{x}}^{G2} + c_{\bar{x}}^{G2}\right)^{1/2} / \left|\vec{B}^G\right|\right]. \tag{21}$$

This expression and similar ones for B_2^{GP} and B_3^{GP} are listed in Table A1.

The process is similar for $B_7^{GP} - B_9^{GP}$. Instead of using $\hat{b}^G$ we use $\hat{n}^G$ from Eq.(5), the normal to the plane containing the object's path, to give

$$\theta_\xi = \sin^{-1}\left(\frac{\left|\vec{A}\times\hat{n}^G\right|}{\left|\vec{A}\right|\left|\hat{n}^G\right|}\right), \xi = 7,8,9. \tag{22}$$

For $B_7^{GP} = \hat{i}^G \cdot \hat{k}^P = \cos\theta_7$,

$$\hat{i}^G \times \hat{n}^G = n_j^G \hat{k}^G - n_k^G \hat{j}^G$$
$$\left|\hat{i}^G \times \hat{n}^G\right| = \left(n_j^{G2} + n_k^{G2}\right)^{1/2} \tag{23}$$
$$\left|\hat{i}^G\right| = \left|\hat{n}^G\right| = 1 \quad,$$

which gives

$$\theta_7 = \sin^{-1}\left[\left(n_j^{G2} + n_k^{G2}\right)^{1/2}\right]. \tag{24}$$

This expression and the formulas for B_8^{GP} and B_9^{GP} are listed in Table A1.

For $B_4^{GP} - B_6^{GP}$, the procedure is somewhat more complicated. We note that the cross product of the known vector $\hat{b}^G$ (parallel to the path axis x^P) and unknown unit vector $\hat{c}^G$ parallel to the path axis y^P will produce a vector that is normal to the plane containing the path. Thus for

$$\hat{c}^G = c_i^G \hat{i}^G + c_j^G \hat{j}^G + c_k^G \hat{k}^G, \tag{25}$$

we have

$$\left| \hat{b}^G \times \hat{c}^G \right| = \left| \hat{b}^G \right| \left| \hat{c}^G \right| \sin\theta = 1 , \tag{26}$$

where

$$\hat{b}^G \times \hat{c}^G = \left(b_j^G c_k^G - b_k^G c_j^G \right) \hat{i}^G + \left(b_k^G c_i^G - b_i^G c_k^G \right) \hat{j}^G + \left(b_i^G c_j^G - b_j^G c_i^G \right) \hat{k}^G . \tag{27}$$

Moreover,

$$\begin{aligned} \hat{b}^G \cdot \hat{c}^G &= \left| \hat{b}^G \right| \left| \hat{c}^G \right| \cos\theta = 0 \\ &= b_i^G c_i^G + b_j^G c_j^G + b_k^G c_k^G \end{aligned} \tag{28}$$

and

$$\begin{aligned} \hat{n}^G \cdot \hat{c}^G &= \left| \hat{n}^G \right| \left| \hat{c}^G \right| \cos\theta = 0 \\ &= n_i^G c_i^G + n_j^G c_j^G + n_k^G c_k^G \end{aligned} . \tag{29}$$

Solving Eqs.(26)–(29) simultaneously gives

$$\begin{aligned} c_i^G &= \pm \left[\left(\gamma b_j^G + \beta b_k^G \right)^2 + \left(b_k^G - \gamma b_i^G \right)^2 + \left(\beta b_i^G + b_j^G \right)^2 \right]^{-1/2} \\ c_j^G &= -\beta c_i^G \\ c_k^G &= \gamma c_i^G \quad , \end{aligned} \tag{30}$$

where

$$\begin{aligned} \beta &= \frac{b_i^G - b_k^G \dfrac{n_i^G}{n_k^G}}{b_j^G - b_k^G \dfrac{n_j^G}{n_k^G}} \\ \gamma &= \left(\beta n_j^G - n_i^G \right) / n_k^G \quad . \end{aligned} \tag{31}$$

Using Eqs.(30) and (31) in Eq.(25), $B_4^{GP} - B_6^{GP}$ can be obtained following the

procedure for $B_1^{GP} - B_3^{GP}$ and $B_7^{GP} - B_9^{GP}$. Thus, θ is

$$\theta_\xi = \sin^{-1} \left(\frac{\left| \vec{A} \times \hat{c}^G \right|}{\left| \vec{A} \right| \left| \hat{c}^G \right|} \right) , \xi = 4, 5, 6 \tag{32}$$

and $B_4^{GP} = \hat{i}^G \cdot \hat{j}^P = \cos\theta_4$ with

$$\hat{i}^G \times \hat{c}^G = c_j^G \hat{k}^G - c_k^G \hat{j}^G$$
$$\left|\hat{i}^G \times \hat{c}^G\right| = \left(c_j^{G2} + c_k^{G2}\right)^{1/2} \tag{33}$$
$$\left|\hat{i}^G\right| = \left|\hat{c}^G\right| = 1$$

to yield

$$\theta_\xi = \sin^{-1}\left[\left(c_j^{G2} + c_k^{G2}\right)^{1/2}\right], \xi = 4,5,6. \tag{34}$$

This and similar expressions for $B_4^{GP} - B_6^{GP}$ are listed in Table A1.

Table A1. Cosines of the angles between the global- and path-coordinate axes for path on plane intersecting global-coordinate axes x^G, y^G, z^G at the points a^G, b^G and c^G.

Cosine of angle	Value of θ for test problem
B_1^{GP}	$\sin^{-1}\left[\left(b_{\bar{x}}^{G2} + c_{\bar{x}}^{G2}\right)^{1/2} / \left|\vec{B}^G\right|\right]$
B_2^{GP}	$\sin^{-1}\left[\left(a_{\bar{x}}^{G2} + c_{\bar{x}}^{G2}\right)^{1/2} / \left|\vec{B}^G\right|\right]$
B_3^{GP}	$\sin^{-1}\left[\left(a_{\bar{x}}^{G2} + b_{\bar{x}}^{G2}\right)^{1/2} / \left|\vec{B}^G\right|\right]$
B_4^{GP}	$\sin^{-1}\left[\left(c_j^{G2} + c_k^{G2}\right)^{1/2}\right]$
B_5^{GP}	$\sin^{-1}\left[\left(c_i^{G2} + c_k^{G2}\right)^{1/2}\right]$
B_6^{GP}	$\sin^{-1}\left[\left(c_i^{G2} + c_j^{G2}\right)^{1/2}\right]$
B_7^{GP}	$\sin^{-1}\left[\left(n_j^{G2} + n_k^{G2}\right)^{1/2}\right]$
B_8^{GP}	$\sin^{-1}\left[\left(n_i^{G2} + n_k^{G2}\right)^{1/2}\right]$
B_9^{GP}	$\sin^{-1}\left[\left(n_i^{G2} + n_j^{G2}\right)^{1/2}\right]$

Stipulated input parameters for Test Model 3 are listed in Table 7. Table A2 contains

several calculated values, including those that also appear in Table 8. Table A3 provides

unit-vector values for Test Model 3.

Table A2. Test Model 3 calculated input values for Box 1.

Quantity	Equation	Box 1 data
O_{Az}^{G} (cm)	Eq.(10)	6.0d2
$a_{\bar{x}}^{G} = -x_{AOR}^{G}$ (cm)	Eq.(13)	-1.0d4
$b_{\bar{x}}^{G} = b^{G} - y_{AOR}^{G}$ (cm)	Eq.(13)	1.3d4
$c_{\bar{x}}^{G} = -z_{AOR}^{G}$ (cm)	Eq.(13)	-6.0d2
$s_{POI} = \rho\left(a_{\bar{x}}^{G2} + b_{\bar{x}}^{G2} + c_{\bar{x}}^{G2}\right)^{-1/2}$ (cm)	Eq.(17)	0.268093401d0
O_{x}^{G} (cm)	Eq.(15)	7.31906599d3
O_{y}^{G} (cm)	Eq.(15)	1.54852142d4
O_{z}^{G} (cm)	Eq.(15)	4.39143959d2

Table A3. Test Model 3 unit-vector values for path on plane intersecting global-

coordinate axes x^{G}, y^{G}, z^{G} at the points a^{G}, b^{G} and c^{G}.

Quantity	Figure Equation	Value
b_{i}^{G} in $\hat{b}^{G} = b_{i}^{G}\hat{i}^{G} + b_{j}^{G}\hat{j}^{G} + b_{k}^{G}\hat{k}^{G}$ (cm)	Eq.(14)	-0.609303185
b_{j}^{G} in $\hat{b}^{G} = b_{i}^{G}\hat{i}^{G} + b_{j}^{G}\hat{j}^{G} + b_{k}^{G}\hat{k}^{G}$ (cm)	Eq.(14)	0.792094140
b_{k}^{G} in $\hat{b}^{G} = b_{i}^{G}\hat{i}^{G} + b_{j}^{G}\hat{j}^{G} + b_{k}^{G}\hat{k}^{G}$ (cm)	Eq.(14)	-0.036558191
n_{i}^{G} in $\hat{n}^{G} = n_{i}^{G}\hat{i}^{G} + n_{j}^{G}\hat{j}^{G} + n_{k}^{G}\hat{k}^{G}$ (cm)	Eq.(5)	0.692635645
n_{j}^{G} in $\hat{n}^{G} = n_{i}^{G}\hat{i}^{G} + n_{j}^{G}\hat{j}^{G} + n_{k}^{G}\hat{k}^{G}$ (cm)	Eq.(5)	0.554108516
n_{k}^{G} in $\hat{n}^{G} = n_{i}^{G}\hat{i}^{G} + n_{j}^{G}\hat{j}^{G} + n_{k}^{G}\hat{k}^{G}$ (cm)	Eq.(5)	0.461757097
c_{i}^{G} in $\hat{c}^{G} = c_{i}^{G}\hat{i}^{G} + c_{j}^{G}\hat{j}^{G} + c_{k}^{G}\hat{k}^{G}$ (cm)	Eq.(25)	-0.386012296
c_{j}^{G} in $\hat{c}^{G} = c_{i}^{G}\hat{i}^{G} + c_{j}^{G}\hat{j}^{G} + c_{k}^{G}\hat{k}^{G}$ (cm)	Eq.(25)	-0.256028563
c_{k}^{G} in $\hat{c}^{G} = c_{i}^{G}\hat{i}^{G} + c_{j}^{G}\hat{j}^{G} + c_{k}^{G}\hat{k}^{G}$ (cm)	Eq.(25)	0.886252719

Values for $B_1^{GP} - B_9^{GP}$ are listed in Table A4.

Table A4. Test problem cosines of the angles between the global- and path-coordinate axes.

B_1^{GP}	-0.609303185
B_2^{GP}	0.792094140
B_3^{GP}	-0.036558191
B_4^{GP}	-0.386012296
B_5^{GP}	-0.256028563
B_6^{GP}	0.886252719
B_7^{GP}	0.692635645
B_8^{GP}	0.554108516
B_9^{GP}	0.461757097

LIST OF TABLE CAPTIONS

LIST OF FIGURE CAPTIONS

Figure 1. Test Model 1. Box 1 (red) and Box 2 (dark blue) undergoing rectilinear translation at t=0, 5, and 10 s. Locations in "k" thousands of cm.

Figure 2. Test Model 2. Box 1 undergoing curvilinear rotation at t=0, 1.66s, 3.33, 5, 6.66, 8.33, and 10 s. Locations in "k" thousands of cm. The plot view is the $x^G - y^G$ plane at $z^G = 12$ cm.

Figure 3. Test Model 2. Model geometry at t = 6.9 s. Box 1 (red) is undergoing curvilinear rotation, while Box 2 (dark blue) experiences rectilinear translation as moves through the plot plane. Locations in "k" thousands of cm. The plot view is the $x^G - y^G$ plane at $z^G = 12$ cm.

Figure 4. Test Model 2. Geometry at t = 0, 5.15, 5, 9.85, and 10 s. Box 1 (red) experiencing curvilinear rotation, Box 2 (dark blue) undergoing rectilinear translation. Locations in "k" thousands of cm. The plot view is the $x^G - z^G$ plane at $y^G = 0$ cm.

Figure 5. Test Model 3 path for Box 1. Object curvilinear rotation about a fixed axis in the plane intersecting the points $x^G = a^G$, $y^G = b^G$, $z^G = c^G$. $\vec{O}^G$ and $\vec{O}^G_A$ are the object's location at time $t = 0$ and axis of rotation, respectively. The radius-of-curvature is $\rho = \left| \vec{r}^G(t) \right|$, which is constant. The object starts at $\vec{O}^G$ with velocity $\vec{v}^P$. The path is oriented in terms of the cosines of the angles $B_1^{GP} - B_9^{GP}$ between the global-coordinate axes x^G, y^G, and z^G and the path's axes x^P, y^P, and z^P.

Figure 6. Test Model 3. Box 1 undergoing curvilinear rotation in tilted plane at t=0,

1.66s, 3.33, 5, 6.66, 8.33, and 10 s. Axis-of-rotation O_{Ax}^{G} = 10000 cm, O_{Ay}^{G} = 12000 cm,

O_{Az}^{G} =600 cm is located at the center of each figure. Box 1 locations are given in Table 10.

Figure 7. Test Model 4. Box 1 (red) and Box 2 (dark blue) motion in y^{G} –z^{G} plane at t=0,

6, 7, 8, 9, 10 s. Locations in "k" thousands of cm.

Figure 8. Test Model 4. Box 1 (red) and Box 3 (light blue) motion in x^{G} – y^{G} plane at 1-

second intervals from t=0 to 10 s. Locations in "k" thousands of cm.

Figure 9. MCNP6 moving target model extending the Beddingfield and Cecil (1998)

experimental setup. In the irradiation calculation, a beam source emits 0.025-eV neutrons

towards the target to induce fission in the HEU or Pu target. A surface-source file is

created for delayed gammas emitted between 1050–1400 s for HEU and 1100–1450 s for

Pu after fission. In the measurement calculation, the surface source is read and

transported to interact with the HPGe detector (lower image). Detector specs (radius =

1.4 cm, height = 4.50 cm) from Knoll (2000).

Figure 10. HEU delayed-gamma emission spectrum. Lower: MCNP6 pulse-height

("F8") tally. Upper: Measured (Beddingfield and Cecil 1998, Fig. 2, reprinted with

permission).

Figure 11. Mesh tally (photons/cm^2-source neutron) of prompt-gamma emission from the moving HEU target (axes in cm).

Figure 12. Mesh tally (photons/cm^2-source neutron) of prompt- and delayed-gamma emission from the moving HEU target (axes in cm).

Figure 13. Mesh tally (photons/cm^2-source neutron) of delayed-gamma emission from the moving HEU target at 7.5 s or later (axes in cm).

Figure 14. Mesh tally (photons/cm^2-source neutron) of delayed-gamma emission between 1050 and 1400 s following fission from moving HEU target (axes in cm).

Figure 15. Mesh tally (photons/cm^2-source neutron) of delayed-gamma emission from the moving HEU target between 1050 and 1400 s (axes in cm) for 1000 source-neutron histories.

Figure 16. Plutonium delayed-gamma emission spectrum. Lower: MCNP6 pulse-height ("F8") tally. Upper: Measured (Beddingfield and Cecil, 1998, Fig. 2, reprinted with permission).

Figure 17. Mesh tally (photons/cm^2-source neutron) of prompt-gamma emission from the moving plutonium target (axes in cm).

Figure 18. Mesh tally (photons/cm^2-source neutron) of prompt- and delayed-gamma emission from the moving plutonium target (axes in cm).

Figure 19. Mesh tally (photons/cm^2-source neutron) of delayed-gamma emission from the moving plutonium target at 7.5 s or later (axes in cm).

Figure 20. Mesh tally (photons/cm^2-source neutron) of delayed-gamma emission between 1050 and 1400 s following fission from moving plutonium target (axes in cm).